1 # First Atmospheric Aerosol Monitoring Results from Geostationary
2 # Environment Monitoring Spectrometer (GEMS) over Asia

3 Yeseul Cho[1], Jhoon Kim[1], Sujung Go[2,3], Mijin Kim[4], Seoyoung Lee[2,3], Minseok Kim[1], Heesung Chong[5],
4 Won-Jin Lee[6], Dong-Won Lee[6], Omar Torres[3], Sang Seo Park[7]

5 [1]Department of Atmospheric Sciences, Yonsei University, Seoul, Republic of Korea

6 [2]Goddard Earth Sciences Technology and Research (GESTAR) II, University of Maryland, Baltimore County, Baltimore, MD
7 21250, USA

8 [3]NASA Goddard Space Flight Center, Greenbelt, MD, USA

9 [4]Goddard Earth Sciences Technology and Research (GESTAR) II, Morgan state university, Baltimore, MD 21251, USA

10 [5]Center for Astrophysics | Harvard & Smithsonian, Cambridge, MA 02138, USA

11 [6]National Institute of Environmental Research, Incheon, Republic of Korea

12 [7]Department of Civil, Urban, Earth and Environmental Engineering, Ulsan National Institute of Science and Technology,
13 Ulsan, Republic of Korea

14

15 *Correspondence to*: Jhoon Kim (jkim2@yonsei.ac.kr)

16 **Abstract.** Aerosol optical properties have been provided from the Geostationary Environment Monitoring Spectrometer
17 (GEMS). It is the world's first geostationary earth orbit (GEO) satellite instrument designed for atmospheric environmental
18 monitoring. This study describes improvements to the GEMS aerosol retrieval algorithm (AERAOD). These include spectral
19 binning, surface reflectance estimation, cloud masking, and post-processing. Furthermore, the study presents validation results.
20 These enhancements are aimed at providing more accurate and reliable aerosol monitoring results for Asia. The adoption of
21 spectral binning in the lookup table (LUT) approach reduces random errors and enhances the stability of the satellite
22 measurements. In addition, we introduce a new high-resolution database for surface reflectance estimation based on the
23 minimum reflectance method adapted to the GEMS pixel resolution. Monthly background aerosol optical depth (BAOD)
24 values are used to consistently estimate the hourly GEMS surface reflectance. Advanced cloud-removal techniques are
25 implemented to significantly improve the effectiveness of cloud detection and enhance the quality of aerosol retrieval. An
26 innovative post-processing correction method based on machine learning is introduced to address artificial diurnal biases in
27 aerosol optical depth (AOD) observations. This study investigates specific aerosol events. It highlights capability of GEMS to
28 monitor and provide insights into hourly aerosol optical properties during various atmospheric events. The performance of the
29 GEMS AERAOD products is validated against the Aerosol Robotic Network (AERONET) and Cloud-Aerosol Lidar with
30 Orthogonal Polarization (CALIOP) data for the period from November 2021 to October 2022. The GEMS AOD demonstrates
31 a strong correlation with the AERONET AOD (R = 0.792). However, it exhibits bias patterns including underestimation of
32 high AOD values and overestimation in low AOD conditions. Different aerosol types (highly absorbing fine, dust, and non-
33 absorbing) exhibit distinct validation results. The GEMS single scattering albedo (SSA) retrievals agree well with the
34 AERONET data within reasonable error ranges, with variations observed among the aerosol types. For GEMS AOD exceeding
35 0.4 (1.0), 42.76% (56.61%) and 67.25% (85.70%) of GEMS SSA data points fall within the ±0.03 and ±0.05 error bounds,
36 respectively. Model-enforced post-processing correction improved the GEMS AOD and SSA performances, thereby reducing
37 the diurnal variation in biases. The validation of the GEMS aerosol layer height (ALH) retrievals against the CALIOP data
38 demonstrates a good agreement, with a mean bias of -0.225 km, and 55.29% (71.70%) of data within ±1 km (1.5 km).

39

1 Introduction

The regional and global monitoring of aerosol optical properties (AOPs) was conducted using satellite measurements. Low earth orbit (LEO) instruments such as the Advanced Very High-Resolution Radiometer (AVHRR), Moderate Resolution Imaging Spectroradiometer (MODIS), Multiangle Imaging Spectro Radiometer (MISR), Visible Infrared Imaging Radiometer Suite (VIIRS), and Sea-viewing Wide Field-of-view Sensor (SeaWiFS), can provide daily aerosol properties for the global domain (Hsu et al.,2004,2006,2017,2019; Jackson et al., 2013; Jethva et al.,2007; Levy et al., 2013; Lyapustin et al., 2018; Martonchik et al., 2009; Remer et al., 2005). While significant diurnal variations in AOPs have been observed at daily and local scales, emphasizing the importance of geostationary satellite measurements for both air quality and climate studies, the temporal resolutions of LEO satellites (typically 1 day) have limitations in investigating the diurnal variation and transboundary transportation of aerosols (Lennartson et al., 2018; Zhang et al., 2018). Geostationary earth orbit (GEO) instruments such as the Advanced Baseline Imager (ABI), Geostationary Ocean Color Imager (GOCI), GOCI-II, Meteorological Imager (MI), and Advanced Himawari Imager (AHI), have contributed to the operational monitoring of the continuous spatio-temporal variations in AOPs at continental spatial scales with temporal resolutions of minutes to hours using the visible and near-infrared channel (Choi et al., 2018; Kim et at., 2016; Kondragunta et al., 2020; Lee et al., 2023; Yoshida et al., 2018).

Besides spatial and temporal resolutions, another critical consideration for satellite aerosol retrievals is channel specification. Every above-mentioned instrument except GOCI-II uses only visible (Vis) and near-infrared channels. However, near-ultraviolet (UV) spectral region uniquely leverages its sensitivity to aerosol absorption. Thereby, it provides valuable insights into aerosol optical properties. A major advantage of near-UV measurements is that the surface reflectance in the near-UV region is darker than that in the visible region. This enables the derivation of AOPs over a bright surface. In addition, observations in the UV region are sensitive to aerosols' radiative absorption and aerosol layer height (ALH) information because Rayleigh scattering is reduced below the aerosol layer owing to aerosol attenuation (Kayetha et al., 2022; Torres et al., 2005).

The Ozone Monitoring Instrument (OMI) serves as an example of an LEO sensor that utilizes UV wavelengths for aerosol retrievals. It has measured radiances in the 270–500 nm spectral range and offered global coverage at a spatial resolution of 13×24 km at nadir since 2004 (Levelt et al., 2018). OMI employs two aerosol algorithms. The first one, OMAERO (Curier et al., 2008), developed and maintained by the Royal Netherlands Meteorological Institute (KNMI), is a multiwavelength algorithm that relies on spectral fitting procedures to derive aerosol properties. The other is the OMI near-UV aerosol retrieval algorithm (OMAERUV). It focuses on retrieving key atmospheric aerosol properties including the aerosol optical depth (AOD), single scattering albedo (SSA), and absorbing aerosol index (AI) (Torres et al., 2007).

The OMAERUV algorithm has its heritage in the Total Ozone Mapping Spectrometer (TOMS) aerosol retrieval algorithm. It uses reflectance measurements at 354 and 388 nm to determine the AOD and SSA using the two channel inversion method (Torres et al., 2002; Torres et al., 2007). The global statistics reported by Ahn et al. (2014) indicate a correlation coefficient (R) of 0.81. However, OMAERUV provides a lower R (0.63) over Central and East Asia (Zhang et al., 2015). In addition, the Tropospheric Monitoring Instrument (TROPOMI) aerosol algorithm (TropOMAER) was developed as an adaptation of OMAERUV. A comparison between Aerosol Robotic Network (AERONET) and TropOMAER AOD at 12 locations yielded an R of 0.82 and a root mean square error (RMSE) of 0.19 (Torres et al., 2020).

The Geostationary Environment Monitoring Spectrometer (GEMS) is the first UV-Vis hyperspectral satellite instrument in a GEO. It is onboard the Geostationary Korea Multi-Purpose Satellite-2B (GEO-KOMPSAT-2B or GK-2B). GEMS was launched on February 19, 2020 (Kim et al., 2020). The objective of the GEMS mission is to monitor the hourly air quality in Asia (5°S–45°N, 75–145°E) with a fine spatial resolution (3.5×7.7 km² at Seoul, South Korea). GEMS provides hyperspectral

81   measurements covering 300–500 nm at a spectral resolution of 0.6 nm. Considering the solar zenith angle (SZA), the GEMS

82   east–west scan profiles are between morning, noon, and afternoon following the sunlit part of the globe to cover the full field

83   of regard (FOR). The GEMS aerosol retrieval (AERAOD) algorithm is based on OMAERUV algorithm and the optimal

84   estimation (OE) method by finding the optimized values of AOD, SSA, and ALH from GEMS measurements at six

85   wavelengths (354, 388, 412, 443, 477, and 490 nm). In order to overcome the challenge posed by the limited degree of freedom

86   for signal in the GEMS wavelength range, this algorithm employs the two channel inversion method that is used in the

87   OMAERUV algorithm to retrieve AOD and SSA. Subsequently, these retrievals are used as the first guesses for the OE method

88   (Kim et al., 2018). The six wavelengths in the UV-Vis region contain information regarding the aerosol absorption in the UV

89   region and the absorption bands of the oxygen dimer (O_2-O_2) at 477 nm. This method was tested using the OMI Level 1 data

90   and was used to derive key aerosol parameters, including AOD, SSA, ALH, UV, and VisAI (Kim et al., 2018; Go et al., 2020a,

91   2020b). Kim et al. (2018) reported that a comparison between AERONET and GEMS AOD at 26 locations in Asia yielded an

92   R of 0.71 and a RMSE of 0.46. The percentage of GEMS SSA within the expected error range of the AERONET inversion

93   data (±0.03) was denoted by 27.54%. Spectral variations of aerosol absorption in the UV-Vis region were investigated by Go

94   et al. (2020a) and it is applied to GEMS aerosol algorithm. The GEMS AOD demonstrated a strong correlation with the

95   AERONET AOD (R = 0.847 and RMSE = 0.285) and the percentage of GEMS SSA within the expected error of ±0.03

96   increased to 41.64% (Go et al.,2020a). To improve the accuracy of GEMS aerosol retrieval, the use of cloud mask information

97   and total dust confidence index from MODIS IR channels was tested for synergy (Go et al., 2020b).

98   However, as the testbed for the GEMS algorithm was on the LEO platform, the time-dependent retrieval bias had not been

99   observed previously. The diurnal variations in satellite-retrieved AOPs may differ from the actual diurnal variations in the

100   AOPs. This discrepancy ~~can be attributed to~~ the different patterns of bias observed over time among the different geostationary

101   satellites and retrieval algorithms (Choi et al., 2018; Lennartson et al., 2018; Wei et al., 2019; Zhang et al., 2020). This diurnal

102   bias in AOP measurements can originate from various factors such as errors in the surface reflectance assumption used in the

103   retrieval algorithm, calibration issues in the Level 1 data, or the presence of short light paths at noon (Ceamanos et al., 2023).

104   To address this issue, an empirical AOD bias-correction algorithm was developed. This algorithm utilizes the lowest AOD

105   values observed within a 30-day period in conjunction with the background AOD to obtain a smoothed bias curve for each

106   pixel of the ABI AOD data (Zhang et al., 2020). This approach helps mitigate the impact of diurnal bias in satellite AOD

107   retrievals to improve the accuracy by removing artifacts from the retrieval. By applying bias correction methods, more reliable

108   diurnal variations in AOD can be explained. Beyond traditional statistical methods, bias correction methods based on machine

109   learning have started to be proposed. Model-enforced post-processing correction involves the use of a machine learning-based

110   model to predict errors in conventional aerosol retrievals (Lipponen et al. 2021, 2022a, 2022b). This method was trained to

111   learn the relationship between the input parameters of the satellite measurements and the associated retrieval errors. This

112   approach provides a practical and effective method to enhance the accuracy of aerosol retrieval without requiring extensive

113   modifications to existing retrieval algorithms. It leverages machine learning capabilities to improve the reliability and precision

114   of hourly aerosol measurements obtained from GEO satellite observations.

115   In this paper, we report the first aerosol monitoring results including the AOD, SSA, and ALH derived using the GEMS aerosol

116   retrieval algorithm. The remainder of this paper is organized as follows: Section 2 of the paper describes the GEMS data and

117   the aerosol retrieval algorithm. It also highlights the algorithm updates after the GEMS in-orbit test (IOT) period. Section 3

118   discusses post-process correction for near-real-time retrieval. Section 4 discusses the GEMS aerosol monitoring results for

119   dust, biomass burning, and absorbing aerosol events over Asia. Section 5 presents an evaluation of the retrieved GEMS AOD,

120   SSA, and ALH retrievals against AERONET and CALIOP data. Section 6 presents the summary and future work.

121

Atmospheric
Measurement
Techniques
Discussions

Open Access

EGU

122   2 Data and GEMS aerosol algorithm

123   2.1 Data description

124   2.1.1 GEMS normalized radiance

125   GEMS operation process provides Level-1C (L1C) dataset in purpose of improving the efficiency of Level 2 algorithm process

126   by combining parameters dispersed in different files into one file. In this study, The aerosol retrieval algorithm used radiances

127   only with the quality flags of 0 (Good) or 2 (interpolated radiances), determined by the "bad_pixel_mask" variable. Rather

128   than GEMS irradiance, we used the KNMI solar reference spectrum to calculate the GEMS-normalized radiance (Dobber et

129   al., 2008). The GEMS irradiance is within the range of -5% to -20% compared with the KNMI solar reference spectrum. It still

130   requires further improvement in L1 processing. To account for the spectral characteristics of the instrument, the KNMI solar

131   reference spectrum is convolved with the GEMS spectral response function. GEMS-measured irradiances are planned to be

132   employed when an improved version of the Sun L1C product is released by the National Institute of Environmental Research

133   (NIER).

134   Normalized radiances are defined in the following equation:

135    $N_\lambda = \frac{I_\lambda}{ESD \ x E_\lambda}$ (1)

136   where I, E, ESD, and λ are the GEMS radiance, KNMI solar reference spectrum, earth–sun distance correction factor, and

137   wavelength (354, 388, 412, 443, 477, and 490 nm), respectively. The spectral radiance and irradiance were spectrally binned

138   and averaged within ±2.2 nm from each wavelength to enhance measurement signals. Additionally, earth–sun distance

139   correction was used to calculate the normalized radiance.

140

141   2.1.2 AERONET

142   AERONET is a global ground-based remote-sensing network that measures aerosol optical, microphysical and radiative

143   properties (Giles et al., 2019; Holben et al., 1998; Sinyuk et al., 2020). The measurement systems use Cimel sun photometers

144   to measure the solar irradiances at eight wavelengths ranging from 340 to 1020 nm and sky radiances at four wavelengths

145   ranging from 440 to 1020 nm. The AERONET data provide global aerosol information including the spectral AOD and

146   inversion products such as the SSA, aerosol size distribution, and refractive index. The uncertainties in AODs are wavelength-

147   dependent. It is approximately 0.01 (Vis) to 0.02 (Near-UV) in direct sun measurements (Dubovik et al., 2002). The

148   uncertainties of SSA are ±0.03 when AOD exceeds 0.4 at 440 nm (Dubovik et al., 2002). For the evaluation of GEMS AOD

149   and SSA data from November 2021 to October 2022, we used AERONET V3 Level 1.5 data for AOD and AERONET V3

150   Level 1.5 hybrid inversion data for SSA from all sites within the entire GEMS domain.

151

152   2.1.3 CALIOP

153   The CALIOP instrument is a two-wavelength polarization-sensitive lidar on the Cloud-Aerosol Lidar and Infrared Pathfinder

154   Satellite Observations (CALIPSO) satellite. It was launched on April 28, 2006 (Winker et al., 2009). CALIOP monitors the

155   global vertical profiles of aerosols and clouds by measuring three signals: the backscatter intensity at 1064 nm and the

156   orthogonally polarized components of the backscattered signal at 532 nm.

157   Quantitative scattering information from CALIOP instruments was used as reference data for validating the ALH obtained

158   from passive sensors (Xu et al., 2017; Xu et al., 2019; Nanda et al., 2020; Park et al., 2023). We used CALIPSO Lidar Level

159   2 Aerosol Profile V3-41 data to validate the GEMS ALH. CALIOP profiles of the extinction coefficient (β_{ext}) at the 532 nm

Atmospheric
Measurement
Techniques
Discussions
Open Access
EGU

160   channel were utilized to calculate the CALIOP ALH using the following equation:

161    $$Z_{aer} = \sum_{i-1}^{n} H(i) \left[\frac{\beta_{ext}(i)}{\sum_{i=1}^{n} \beta_{ext}(i)} \right] \tag{2}$$

162   where $\beta_{ext}(i)$ is the CALIOP profile of the 532 nm extinction coefficient at height $H(i)$ and n is the number of layers.

163

164   2.2 GEMS AERAOD retrieval algorithm

165   2.2.1 Aerosol optical properties retrieval algorithm for GEMS

166   The GEMS AERAOD algorithm produces AOD, SSA, and ALH via the OE method. The preliminary GEMS AERAOD was
167   developed using OMI L1B normalized radiance (Kim et al., 2018; Go et al., 2020a, 2020b). After the launch, the algorithm
168   was tested using the GEMS observation during the IOT period, and several parts of the algorithm were updated. This section
169   briefly describes the GEMS AERAOD algorithm; AERAOD L2 data; and updates including the Look-Up Table (LUT), cloud
170   masking procedure, surface reflectance estimation, and post-processing after the IOT period. The general flow of the GEMS
171   AERAOD retrieval algorithm is illustrated in Figure 1.

172   GEMS algorithm adopts a LUT approach to optimize computation efficiency. The LUT is calculated assuming AOPs of three
173   aerosol types by using a radiative transfer model (RTM), the Vector Linearized Discrete Ordinate Radiative Transfer code
174   (VLIDORT) (Spurr, 2006). The AOPs of Highly absorbing fine (HAF), Dust, and Non-absorbing (NA) are integrated from
175   AERONET inversion data and are applied for the RTM simulation. The details of the updated LUT are described in section
176   2.1.2. The preliminary algorithm used the OMI climatology Lambertian equivalent reflectance (OMLER v003) datasets as
177   surface reflectance, but for the GEMS AERAOD algorithm, GEMS L2 surface reflectance at 354, 388, 412, 443, 477, and 490
178   nm are obtained by minimum reflectance method. The details of surface reflectance estimation are described in section 2.1.3.

179   The GEMS AERAOD provides UV and visible (Vis) AI to indicate the qualitative radiative absorptivity and particle size
180   information, respectively (Torres et al., 2002). The GEMS UVAI and VisAI were calculated using the following equations:

181    $$AI = -100 \left[\log\left(\frac{N_{\lambda_1}}{N_{\lambda_2}} \right)_{meas} - log\left(\frac{N_{\lambda_1}(LER_{\lambda_1})}{N_{\lambda_2}(LER_{\lambda_2})} \right)_{calc} \right] \tag{3}$$

182   where N_{λ_1} and N_{λ_2} are the normalized radiances at the 354/388 (477/490) nm wavelength pair for UVAI and VisAI,
183   respectively. The subscripts *meas* and *calc* represent the measured and calculated normalized radiances, respectively.

184   Aerosol type among HAF, dust and NA is selected using the UVAI and VisAI. The NA type was detected by a negative UVAI
185   value. The dust and HAF types were distinguished by VisAI. When both AIs were positive, the dust type was selected. Sun
186   glint and cloud masking leave only the pixels appropriate for aerosol retrieval. The glint mask is set for glint angles less than
187   35°. The details of the cloud-masking procedure are described in Section 2.1.4. The *a priori* states of AOD and SSA at 443 nm
188   were obtained by two-channel inversion with neighboring wavelengths (354 and 388 nm) over both land and ocean. The
189   assumption was that the climatology of ALH was based on CALIOP. The a priori states of the AOD and SSA were supplied to
190   solve the Levenberg–Marquardt equation. The optimal ALH was retrieved by fitting the normalized radiance between the
191   measured and calculated values for the OE routine. The details of the GEMS aerosol inversion procedure are described by Kim
192   et al. (2018).

193   To improve the accuracy of near real-time GEMS AOD retrieval, a model-enforced post-process correction step was
194   implemented using a random forest (RF) model. By combining GEMS aerosol retrieval with this post-processing correction
195   model, more reliable and accurate near real-time AOD estimates can be obtained.

2.1.2 LUT calculation

In this study, the AOPs were ~~considered~~ as described by Kim et al. (2018) and Go et al. (2020a). However, the dimensions of the LUT varied (as shown in Table 1) compared with Kim et al. (2018). The nodes for the 412 nm SSA node for NA were added. In addition, the nodes for AOD in the LUT were extended to include the values at 5.0 and 10.0 ~~because the previous maximum node was 3.6. These modifications~~ enable the retrieval of exceptionally severe aerosol events during GEMS observations. The preliminary GEMS AERAOD retrieval algorithm utilized the normalized radiance at six specific monochromatic wavelengths (354, 388, 412, 443, 477, and 490 nm). However, satellite measurements averaged over a specific wavelength range produce more stable values than measurements obtained at individual monochromatic wavelengths. ~~This increased stability is attributed~~ to the averaging of random errors (i.e., instrument noise). Consequently, a spectral-binning LUT approach was employed to reduce random errors and improve the stability of the measurements. This allowed for more reliable and consistent observations. Compared with monochromatic wavelengths, the spectral binning method is computationally intensive. Therefore, the calculations were performed using the Mie theory without considering the non-sphericity of the dust. The process of spectral binning LUT in the GEMS aerosol algorithm involves three steps: 1) A reference spectrum is generated using an RTM, which provides a spectral interval of 0.1 nm. 2) The calculated spectrum is convolved with the GEMS spectral response function and resampled to the target spectral grids with a resolution of 0.2 nm. (Kang et al., 2020). 3) The resampled spectrum is averaged at intervals of ±2.2 nm at six central wavelengths (354, 388, 412, 443, 477, and 490 nm) and saved in the LUT. This range is selected to account for the calculation capacity and reduce the impact of random errors. During the retrieval process, the GEMS L1C normalized radiances after being averaged at intervals of ±2.2 nm at six central wavelengths are compared with the calculated spectrum in the LUT. By these steps, the spectral binning LUT aims to generate more stable retrieval results for aerosol properties.

2.1.3 Surface reflectance estimation

In this study, several improvements were introduced. These include an updated GEMS surface reflectance estimation. The preliminary GEMS AERAOD retrieval algorithm used the OMI surface reflectance climatology data product OMLER v003 (Kleipool et al. 2008), with a spatial resolution of $0.5 \times 0.5°$. The limitation of the previous surface reflectance data was its coarse spatial resolution compared with that of GEMS pixels. This resulted in discontinuities in the GEMS AOPs owing to spatial resolution differences. To address this limitation, the updated GEMS surface reflectance has a finer spatial resolution $(0.1 \times 0.1°)$. This closely aligns with the GEMS pixel resolution. This enhancement enables a more accurate aerosol retrieval at the pixel level. The compiled hourly surface reflectance indirectly reflects the bidirectional reflectance distribution function (BRDF) effect. In addition, a new hourly surface reflectance database was generated using the minimum reflectance method based on the GEMS data. The algorithm adopts the climatological minimum reflectance method for each pixel over a ±15-day window spanning a period of two years. Several tests were performed to evaluate different time windows and methods for constructing accurate surface reflectance. These tests evaluated the effectiveness of using a ±15-day window as well as alternative options such as a previous 30-day window. In addition, different methods including the minimum reflectance and second minimum reflectance approaches were evaluated to determine the most suitable one for generating appropriate surface reflectance values (not included in this study).

The background AOD (BAOD) was considered in the retrieval algorithm. The BAOD represents the baseline level of AOD that is consistently present in a region. Recent studies have shown that incorporating BAOD into an algorithm can reduce the uncertainty associated with satellite-based AOD ~~remote sensing~~ (Kim et al., 2014, 2021). Zhang et al. (2016) estimated BAOD as the lowest fifth percentile of AERONET AOD over a two-year period and improved the performance of the VIIRS aerosol

Atmospheric
Measurement
Techniques
Discussions

Open Access

EGU

237   algorithm. It has been observed that Asia experiences relatively high BAOD values with seasonal variation. For example, at

238   the Dhaka University site, the monthly BAOD over the past two years varied from a minimum of 0.124 in August to a

239   maximum of 0.685 in April. Therefore, considering the seasonal variation in BAOD for atmospheric correction can help

240   mitigate the uncertainty in satellite-derived AOD retrieval, particularly over Asia. The monthly BAODs were calculated using

241   the following equation for each $0.1 \times 0.1°$ box from November 2020 to October 2021:

242    $$\tau_{grid,b,m}(lat, lon) = \sum_i W_i \tau_{b,m,i}, \sum_i W_i \qquad (4)$$

243   where $\tau_{grid,b,m}(lat, lon)$ is the interpolated BAOD 443 nm at *(lat, lon)* in month *m*. W_i is the inverse distance weighting

244   function, which is defined as $e^{-d_i(lat,lon)/d_0}$. $d_i(lat, lon)$ is the distance between the AERONET site and GEMS pixel and d_0

245   is a constant, respectively. $\tau_{b,m,i}$ is the lowest fifth percentile of AERONET AOD over a two-year period at AERONET site *i*

246   in month *m*.

247   Figure S1 shows the monthly BAOD obtained based on the AERONET AOD data. Additionally, the fifth percentiles of the

248   AERONET AOD 443 nm values at each AERONET site are plotted as circles for reference. It is evident that regions such as

249   India exhibit a high BAOD of over approximately 0.15 throughout the year, regardless of the month. However, seasonal

250   variations in BAOD occur over the Indochinese Peninsula, Korea, and China. These areas experience heavy pollution from

251   biomass burning during the dry season and dust events from deserts. Both these contribute to increased atmospheric aerosol

252   concentrations. These enhancements, including the use of hourly GEMS surface reflectance and incorporation of monthly

253   BAOD, can result in improved aerosol retrieval.

254

255   2.1.4 Cloud masking procedure

256   The GEMS aerosol algorithm retrieved AOPs only in cloud-free pixels. Clouds exhibit spatial inhomogeneity and higher

257   brightness than aerosols. This study aimed to enhance the cloud-masking process in the GEMS aerosol algorithm by addressing

258   the limitations of previous simple cloud-masking techniques. The previous method relied on a (1) fixed threshold for

259   reflectance at 412 nm and (2) standard deviation test of reflectance within a 3×3 pixel area. To improve the performance of

260   cloud masking, an additional cloud removal technique has been introduced in this study. These tests include the following: (3)

261   470/477 nm normalized radiance ratio test. It involves a threshold test for the ratio of the normalized radiance values at 470

262   nm and 477 nm. This contrasts the presence of clouds using absorption bands of O_2-O_2. (4) The difference between hourly

263   surface reflectance database and the calculated scene reflectivity at 412 nm: Significant differences indicate the presence of

264   clouds (Torres et al., 2013). (5) Standard deviation test of normalized radiance at 477 nm within a 3×3 pixel area: The

265   threshold for this test can vary based on the latitude considering the regional differences in cloud characteristics. (5-1) Standard

266   deviation in 3×3 pixel > *f(latitude)* (5-2) after 3-1, standard deviation in 3×3 pixels > *f(latitude, number of cloud pixels*

267   *detected method (1), (3), (4) in 3×3 pixels)*. A final cloud mask was applied after the aerosol retrieval. This included (6)

268   filtering out high AOD values using a threshold that is a function of the number of cloud pixels detected by methods (1), (3),

269   (4), and (5) in 11×11 pixel over the ocean (Lyapustin et al., 2021). This helps remove residual clouds. By implementing these

270   new methods, the algorithm aims to improve the effectiveness of cloud detection and removal in GEMS pixels.

271

272   3 GEMS post-process correction for the near-real-time retrieval

273   The GEMS AOD exhibited a diurnal bias pattern that fluctuated throughout the day. It formed a U-shape, with a minimum at

274   03:00 UTC (as will be demonstrated in Section 5.1). To improve the accuracy of near real-time GEMS AOD retrieval, a model-

275   enforced post-process correction step was implemented using a random forest (RF) model proposed by Lipponen et al. (2021).

Atmospheric
Measurement
Techniques
Discussions

Open Access
EGU

276 This concept was trained to learn the relationship between the hourly GEMS data and AOD errors (GEMS-AERONET AOD)
277 and to predict the AOD errors at the target time. To enable near real-time retrieval, the proposed method consists of two main
278 parts: modelling and prediction. In the modelling part, the input data for the RF model includes GEMS data (normalized
279 radiances at six wavelengths, scattering angle, viewing zenith angle (VZA), relative azimuth angle (RAA), SZA,UV and VisAI,
280 aerosol type, AOD, and clear fraction (ClearFrac) (which is the ratio of clear-sky pixels to the total pixels within the 0.25°
281 radius from the pixel center)). The data also include auxiliary information such as time, land–sea mask, and elevation. The
282 target data for training were the AOD errors. Each of these was calculated as the difference between the GEMS AOD and
283 AERONET AOD at the corresponding single GEMS pixel where the AERONET site was located. The predictors and target
284 variables were collected for a time window ranging from N days to one day before the target time. After conducting several
285 tests, N was determined to be 30 days. In the prediction part, the input variables including the GEMS data and auxiliary
286 information in the target time were used for the pretrained RF model. Using these inputs, the model predicted the error in the
287 GEMS AOD in near real-time. This predicted error value was then applied to the first retrieved GEMS AOD from the retrieval
288 algorithms. This resulted in the production of the post-processed GEMS AOD.

289 In addition, the diurnal bias pattern in the GEMS SSA also exhibited fluctuations throughout the day, forming a bell shape with
290 a minimum at 03:45 UTC. This is shown in Section 5.2. The post-processing method adopted was similar to that used for AOD.
291 This method was trained to determine the relationship between hourly GEMS data and SSA errors (the difference between
292 GEMS at 443 nm and AERONET SSA at 440 nm) and predict SSA errors for the target time. The key difference between the
293 RF model predicting the AOD error and that predicting the SSA error is as follows: the second model includes the GEMS SSA
294 as an input variable, and then, 19 input parameters are used to construct the RF model.

295 Unlike AOD and SSA, the postprocessing of ALH using an RF model is inherently limited. CALIOP is predominantly used as
296 reference data for ALH. Because CALIOP is an LEO satellite, pixels co-located with GEMS ALH data are available only from
297 03:45 to 07:45 UTC. This renders it inaccessible as a reference hourly dataset covering 22:45–02:45 UTC. Unlike AEROENT,
298 the use of data from ground-based lidar is severely constrained by the limited number of observation stations and restricted
299 geographical areas in which lidars are deployed.

300

301 4 Aerosol events

302 4.1 Dust aerosol event (2022.04.08)

303 Figure 2 present an example of hourly maps of the GEMS aerosol product including AOD, SSA, ALH, UVAI, and VisAI for
304 April 8, 2022. These results are the GEMS AOD and SSA before post-processing. The selected case is for the dust aerosol
305 event over northwestern China. The GEMS false RGB is shown using R (477 nm), G (412 nm), and B (354 nm) bands similar
306 to those of the OMI false RGB method (Levelt et al., 2006).

307 As shown in Figure 2, different retrieval regions with respect to time are shown as the GEMS scan profile varies with the SZA.
308 Overall, the GEMS AOD shows a significantly good agreement with the AERONET AOD measurements. It captures higher
309 values in the Beijing–Hebei–Tianjin (BTH) region and lower values over South Korea and Japan. High GEMS AOD values
310 were evident along the dust plume, attaining two at 06:45 UTC. In the case of SSA, the retrieval results demonstrated a
311 relatively lower accuracy (notably in the BTH region) compared with AOD. In general, from 22:45 to 05:45 UTC, the SSA
312 values displayed good concordance with both AERONET and GEMS SSA. However, from 06:45 to 07:45 UTC, the SSA
313 numbers did not match over Beijing. Compared with the Beijing region, the results are more consistent in the dust plume. The
314 SSA values remained relatively stable at approximately 0.92–0.96 over time. However, the GEMS SSA tended to have a
315 positive bias compared with the AERONET values. This is shown in Section 5.2. The GEMS ALHs were ~3–4 km for the dust

316 plume over the Taklamakan Desert and ~1.0 km over the Beijing region. The GEMS ALH exhibited continuous spatial and

317 temporal patterns. The UVAI provides information regarding the radiative absorption of aerosols. It attained a maximum of

318 four for dust plumes, thereby indicating significant aerosol absorption. However, over Beijing, the SSA was ~1. This indicated

319 a marginal absorption owing to the different aerosol emission source. VisAI provides information on the aerosol size. In regions

320 with a dust plume, the VisAI value was higher than that in the background areas. This indicated the presence of coarse aerosol

321 particles.

323 4.2 Biomass burning event (2022.03.19)

324 Figure 3 illustrates maps of the GEMS aerosol product at 06:45 UTC on March 19, 2022. It represents a biomass-burning event

325 over mainland Southeast Asia. These results were obtained for the GEMS AOD and SSA before post-processing. During the

326 dry season in this region, highly absorbing fine pollution particles are prevalent (Yin et al., 2019). The GEMS AOD > 1.6. This

327 indicated a significant aerosol loading and enhancement during the event. The GEMS SSA was ~0.88. This indicated aerosol

328 absorption during this event. The ALH ranged from 2 to 3 km within the biomass-burning plume. The GEMS ALH was not

329 retrieved along the east-to-west straight line at ~22.5 °N, which are bad pixels in the CCD. The GEMS UVAI showed hotspots

330 and fine features associated with this event. Thus, it captured aerosol absorption in the ultraviolet spectrum. VisAI exhibited

331 higher values than the background. This case study demonstrates that the GEMS provides valuable insights into aerosol

332 properties during specific events such as biomass burning, and can capture temporal and spatial variations in AOD, SSA, ALH,

333 UVAI, and VisAI.

334 Figure 3g shows a comparison of the CALIOP extinction coefficients at 532 nm, the CALIOP ALH, and the GEMS ALH over

335 the CALIOP path (the green line on the GEMS false RGB image in Figure 3a). Figure 3g illustrates a clear relationship between

336 the GEMS AOD and accuracy of GEMS ALH. The accurate retrieval of ALH requires the presence of a sufficient amount of

337 aerosols in the atmosphere. GEMS ALH closely follows the latitudinal variation in CALIOP ALH. As the latitude increased

338 from 18° to 21°, the GEMS ALH followed the CALIOP ALH and showed an increase in altitude. In the latitude range of 24°–

339 28°, the GEMS AOD decreased, and the GEMS ALH exhibited scattered variations owing to weaker signals. In the scatter plot

340 comparing CALIOP ALH and GEMS ALH (Figure 3h), 39.88% of the pixels are within the expected error range of 0.5 km,

341 and 68.10% of the pixels are within the expected error range of 1 km. As the GEMS AOD values decreased, the GEMS ALH

342 pixels were more likely to be outside the expected error range.

344 4.3 Absorbing aerosol event (2021.12.04, 2021.12.23)

345 Figure 4 shows an example of the GEMS AOD before and after post-processing for an absorbing aerosol case over Indo-

346 Gangatic Plane (IGP) at 04:45 UTC on December 4, 2021. During the wintertime in this region, atmospheric haze is prevalent

347 (Ram et al., 2012). Recent studies have shown that primary aerosols and precursors for secondary aerosols emitted from fossil

348 fuel combustion and biomass burning are released into the atmosphere (Singh et al., 2021). Figure 4a shows the GEMS false

349 RGB image with AERONET stations represented by circles. The color indicates the AERONET AOD. Two distinct aerosol

350 plumes are observed. The northwest shows an AOD of ~0.8, whereas the southeast has a value of ~1.3. Figure 4b shows the

351 GEMS AOD data. The spatial distribution of the GEMS AOD is similar to that of the AERONET AOD in Figure 4a. However,

352 the values are marginally lower than those of the AERONET AOD. Meanwhile, the AOD increased after post-processing,

353 particularly in the moderate AOD range (~0.7). Moreover, the GEMS AOD was closer to the AERONET AOD (Figure 4c).

354 Specifically, at the Gandhi_College site (25.871 °N, 84.128 °E) and Lahore (31.480 °N, 74.264 °E), postprocessing resulted

355 in more reasonable values.

356 Figure 5 shows the maps of the GEMS SSA and the GEMS SSA after post-processing for an absorbing aerosol case over India,

357 Bangladesh, and mainland Southeast Asia at 03:45 UTC on December 23, 2021. Figure 5a shows the GEMS false RGB image

358 with AERONET stations represented by circles. The color indicates the AERONET SSA at 440 nm. The AERONET SSA

359 values are ~0.9 in India and Bangladesh, and ~0.93 in Thailand. Before postprocessing, the GEMS SSAs exhibit values of

360 ~0.96 in the Indian region and ~1.0 in the other areas. However, following postprocessing, the GEMS SSA values converged

361 to be more similar to the AERONET SSA values. Nonetheless, a marginal tendency for overestimation remained.

362

363 5 Validation in GEMS AERAOD product

364 This section evaluates the GEMS AOD and SSA at 443 nm according to the aerosol type and measurement time using the

365 AERONET data in the entire GEMS domain. We used AERONET version 3 level 1.5 data to validate both AOD and SSA to

366 ensure a larger dataset for validation purposes. Figure 6 illustrates a map of the AERONET sites used for GEMS AOD and

367 SSA validation, in conjunction with site-specific data counts. The AERONET AOD data generally showed higher counts for

368 South Korea, China, and Taiwan. Meanwhile, sites in South and Southeast Asia typically had fewer data points. Similarly, the

369 number of AERONET SSA data points showed a distribution similar to that of AOD. However, AERONET sites #38, #39, and

370 #47 in India had over 400 validation points. In addition, we retrieved the GEMS ALH and compared it with the CALIPSO

371 level 2 extinction coefficient profiles at 532 nm as well as with the CALIOP ALH defined by Equation (2).

372

373 5.1 Aerosol optical depth

374 In this section, the GEMS AOD at 443 nm is validated against AERONET data across the entire GEMS domain from November

375 1, 2021 to October 31, 2022. The GEMS AOD data were spatially collocated within a 0.25° radius of the AERONET stations

376 and temporally within a 30 min window of the GEMS measurement time. When a specific aerosol type in the GEMS was

377 present in more than 90% of the pixels within the validation radius, an aerosol type validation was conducted.

378 Figure 7 presents the results for all the pixels and each aerosol type (HAF, dust, and NA). The statistics include R, RMSE,

379 mean bias error (MBE), slope, y-offset, Q value indicating the percentage of data points within the maximum (0.1 or 30%

380 AOD) error range, and the Global Climate Observing System (GCOS) requirement (defined as the maximum (0.03 or 10%

381 AOD)). The total GEMS AOD demonstrated a good correlation with the AERONET AOD, with an R of 0.792, RMSE of 0.227,

382 and MBE of 0.038 (Figure 7a). The Q value was calculated to be 54.84%, with 18.39% of the AOD satisfying the GCOS

383 requirements. However, the slope and y-intercept were 0.589 and 0.193, respectively. This indicated an overestimation for a

384 low AERONET AOD and an underestimation for a high AERONET AOD. In the case of a low AERONET AOD, there is

385 evidence of cloud contamination effects. These result in an overestimation of the retrieved GEMS AOD.

386 The validation shows the differences by aerosol type. The HAF type showed the highest R and Q values compared with the

387 other aerosol types (Figure 7b). Pixels that deviated beyond the error range owing to the GEMS AOD underestimation were

388 notably observed in two main categories: sites in the Indian region (which still showed bias notwithstanding the consideration

389 of BAOD) and sites located in Beijing with an AERONET AOD of approximately 2.0 and a GEMS AOD of approximately

390 1.0. Among the three aerosol types, the dust type had the fewest samples, accounting for 1 / 10 of the NA (Figure 7c). The R-

391 value was 0.786, and the slope was the highest among the three types. Pixels that deviated beyond the error range owing to

392 GEMS AOD underestimation were primarily observed in the Indian region. In contrast, pixels exceeding the error range owing

393 to GEMS AOD overestimation were located in Northeast Asia. Currently, GEMS uses the same aerosol model (number-size

394 distribution parameters and real refractive index) over the entire domain for each aerosol type. However, given the varying

395 bias patterns observed in the dust type, it is necessary to consider regional variations in the GEMS aerosol model (and thus,

396 the LUT) in future studies. The NA type was selected most frequently among the three aerosol types (Figure 7d). Figure 7d

397   shows that a significant number of pixels are influenced by cloud contamination, which is particularly evident in regions with

398   low NA AOD values. It appears that the GEMS aerosol cloud masking process requires further improvement, particularly over

399   the ocean. The current cloud-masking process may not effectively distinguish small clouds (i.e., broken clouds) near equatorial

400   regions. This results in an overestimation of the AOD owing to cloud contamination. This phenomenon has been observed

401   frequently at AERONET stations located near the equator. The underestimation of high AOD values in the GEMS aerosol

402   algorithm can be attributed to the effect of the current aerosol model assumption used in the algorithm. This emphasizes the

403   importance of understanding the AOPs to better characterize these in the atmosphere, particularly in the UV region.

404

405   Figure S2 and Table 2 present the hourly AOD validation results and statistical metrics including N, R, slope, y-intercept,

406   RMSE, MBE, Q value, and GCOS. It is important to note that the GEMS varies its E-W scan profile depending on the SZA.

407   Therefore, the sites used for validation may not have remained consistent over time. For example, the AERONET stations

408   around 22:45 UTC and 23:45 UTC were mostly used for validation in the eastern region of GEMS, whereas those around

409   06:45 UTC and 07:45 UTC were expected to be in the western region of GEMS. A systematic error analysis is planned in a

410   future study. Nevertheless, the hourly validation results of the GEMS AOD provide significant insights. The hourly slopes of

411   the GEMS AOD exhibited a diurnal variation, starting at 0.730 at 22:45 UTC; decreasing to 0.534 and 0.555 by 1:45 UTC

412   and 2:45 UTC, respectively; and subsequently increasing to 0.647 and 0.617 at 06:45 and 7:45 UTC, respectively. However,

413   the R-values remained relatively stable over time. Most time intervals exhibited R values of approximately 0.77 or higher

414   except for 22:45. Figure S2 and Table 2 show that the diurnal variation in GEMS AOD did not precisely reflect the actual

415   diurnal AOD variation. Thus, it is necessary to correct and produce a consistent dataset over time to investigate the diurnal

416   variations in aerosol properties. A machine learning model using RF was used to train the hourly dependent error

417   characteristics, remove artifacts in the retrieval processes, and maintain the physical signals.

418   Figure 8a shows the comparison results for GEMS AOD after model-enforced post-processing correction with AERONET

419   data. For near-real-time post-processing correction, data from the past 30 days were used for training. Therefore, these results

420   were evaluated over 11 months: from December 1, 2021, to October 31, 2022. Figure 8a shows that all the statistical metrics

421   improved. In particular, the slope was closer to one at 0.809, and the y-intercept was closer to zero at 0.068. Additionally, R,

422   RMSE, and MBE were 0.899, 0.159, and -0.005, respectively. The Q value and GCOS requirements also improved to 79.13%

423   and 36.08%, respectively. The bias near low AOD values of approximately zero was reduced significantly. Furthermore, the

424   high AOD values were closer to the 1:1 line. Figure 8b shows the bias of the GEMS AODs before and after post-process

425   correction with respect to time for all the AOD pixels. After applying the model-enforced post-process correction to the GEMS

426   AOD data, significant improvements in bias were observed over the diurnal cycle. The original GEMS AOD exhibited an

427   hourly-dependent bias characteristic. It formed a U-shape with a minimum value near noon, 03:45 UTC. However, with the

428   implementation of the model-enforced post-processing correction, the diurnal bias was mitigated effectively. This resulted in

429   a bias value close to zero throughout the day and a decreased standard deviation. Figure 8c illustrates the diurnal variation in

430   the bias of a low AOD (AERONET AOD < 0.4). The GEMS AOD (red circles) exhibited a positive bias of ~0.1. It was mostly

431   corrected to values close to zero after post-processing (blue circles). However, certain positive bias was observed at

432   approximately 22:45 and 23:45 UTC, and at 06:45 and 07:45 UTC. Figure 8d shows the diurnal variation in the bias of high

433   AOD (AERONET AOD > 0.4). The diurnal variation in GEMS AOD (red circles) shows a clear U-shaped pattern with a

434   maximum negative bias of approximately -0.2 at 0.3 UTC. However, after post-processing, the bias was still negative but less

435   than -0.1, which is significantly closer to zero. By incorporating the predicted error, we obtained an improved GEMS AOD

436   that considers the uncertainties and biases inherent in the retrieval process. This approach helps reduce these biases, including

437   a low AOD overestimation, high AOD underestimation, and artificial diurnal bias in near-real-time AOD retrievals. The

438   reduction in artifactual diurnal bias is crucial for ensuring the reliability of hourly GEMS AOD data. This is because it

Atmospheric
Measurement
Techniques
Discussions

439   eliminates time-dependent discrepancies and provides a more representative hourly aerosol distribution. Users can now rely

440   on corrected GEMS AOD data for various applications without being influenced by diurnal variations in the original

441   measurements. Variable importance analysis for the post-processing correction of the GEMS AOD was conducted (Figure S3).

442   GEMS AOD was the most important variable, emphasizing its direct influence on the correction process. VZA and elevation

443   exhibited high importance. However, their significance can be attributed not only to their inherent properties but also to their

444   role in conveying AERONET location-related information. Aerosol type appeared to have less significance in the RF models.

445   This result contrasted with the notable importance of GEMS UVAI and VisAI. This discrepancy can originate from inaccurate

446   aerosol type classification in the GEMS aerosol algorithm.

447

448   5.2 Single-scattering albedo

449   This section presents a comparison of the GEMS SSA at 443 nm with the AERONET SSA at 440 nm in the entire GEMS

450   domain. The validation period and collocation criteria for the AERONET sites were identical to those for the GEMS AOD.

451   Similar to the AOD, when a particular aerosol type in the GEMS was detected for over 90% of the pixels within a 0.25° radius,

452   we performed aerosol-type validation. Figure 9 and Table 3 display the validation results for all pixels and each aerosol type.

453   The statistics including N and percentages are within the expected error ranges (0.03 and 0.05). The uncertainty of SSA is

454   ±0.03 when AERONET AOD 440 nm is over 0.4 (Dubovik et al., 2002). The gray dashed lines indicate an uncertainty envelope

455   of ±0.03 in SSA, whereas the black dashed lines indicate an uncertainty envelope of ±0.05 in SSA. These reference lines help

456   assess the agreement between the GEMS SSA and AERONET data within a reasonable error range. When aerosols are not

457   abundant in the atmosphere, capturing SSA signals from satellite observations is challenging. Therefore, for validation,

458   separate analyses were conducted for the cases where the GEMS AOD > 0.4 (indicated by the red open circles) and the GEMS

459   AOD was > 1.0 (indicated by the blue open circles). Notwithstanding the large uncertainties associated with the satellite

460   measurements, the GEMS aerosol product showed a good overall agreement with the AERONET SSA. When GEMS AOD

461   exceeds 0.4, the percentage of GEMS SSA within the expected error range of ±0.03 is denoted by 42.76%, and that within the

462   expected error range of ±0.05 is denoted by 67.25%. When the aerosol signal is strong (when GEMS AOD exceeds 1.0), the

463   percentage of GEMS SSA within the expected error of ±0.03 (0.05) increases to 56.61% (83.70%). However, the percentage

464   within the expected error range and scatter plots varied depending on the aerosol type. For the HAF type, the SSAs showed

465   the largest spread. This indicated a lower accuracy. It was likely to be a result of an ineffective aerosol-type selection (red

466   circles). However, when AOD exceeds 1.0 (blue circles), these tend to approach the 1:1 line. Moreover, the percentage falling

467   within the expected error range of ±0.03 increases significantly. For the dust type, the GEMS SSA exhibited a positive bias of

468   approximately 0.04 compared with the AERONET SSA (red circles). Similarly, when the AOD exceeds 1.0, these biases

469   decrease, approaching the 1:1 line (blue circles). However, the systematic bias observed in the GEMS SSA for the dust type

470   indicates the need to refine the assumed dust AOPs in the LUT. The NA type in GEMS was observed to have a significantly

471   low variability compared with AERONET SSA. The GEMS SSAs showed values close to one compared with the AERONET

472   data. According to Lee et al. (2010), the NA type is identified when the SSA is above 0.95. However, many NA-type pixels

473   were observed, with AERONET SSA values below 0.95 in the NA type. This indicates potential inaccuracies in the

474   classification of the absorbing and NA GEMS aerosol types. Nevertheless, when the AOD is high (blue circles), these

475   classification errors tend to decrease. This results in values closer to the AERONET SSA.

476   Figure S4 and Table 4 present the hourly SSA validation results and statistic metrics including the N and percentage within

477   the expected error range of ±0.03 (±0.05). The GEMS and AERONET SSA exhibited varying distributions over time. The

478   difference between the GEMS and AERONET SSA was most significant at 03:45 and 04:45 UTC, with a positive bias. This

479   difference decreased at 22:45 and 23:45 UTC or 05:45 and 06:45 UTC (Figure S4). Similar to the GEMS AOD, the GEMS

480   SSA showed diurnal variations. These are also reflected in the EE% values shown in Table 4. At 22:45 and 23:45 UTC, the

Atmospheric
Measurement
Techniques
Discussions

Open Access

EGU

481 percentage within the expected error range of ±0.03 exceeded 60%. However, it reduced to less than 30% at 03:45 and 04:45

482 UTC before increasing again. Further studies are required to understand the bias and accuracy variations in the SSA and

483 improve the retrieval results. This can also be attributed to the shorter path length in the observation geometry when the

484 influence of surface reflectance increases, similar to that in AODs.

485 Figure 10a presents the comparison results for the GEMS SSA after post-process correction and the AERONET data. The

486 near-real-time post-process correction utilized data from the preceding 30 days for training. The validation period was from

487 December 1, 2021, to October 31, 2022. Notably, all the statistical metrics demonstrated improvements. Specifically, the

488 percentage of GEMS SSA falling within the expected error range of ±0.03 was recorded at 68.33%, whereas the percentage

489 within the range of ±0.05 was indicated at 88.86%. Furthermore, the SSA values exhibited a closer alignment with the 1:1

490 line. Figure 10b depicts the difference between the GEMS and AERONET SSA over the measurement time. Notably, the

491 bias pattern observed in the GEMS SSA exhibits artifactual characteristics, thereby forming a bell-shaped curve. In

492 particular, during the time interval from 01:45 to 05:45 UTC, the mean bias of GEMS SSA consistently surpassed the

493 expected error range of ±0.03. However, the implementation of model-enforced post-process correction was demonstrated to

494 be highly effective in mitigating this artificial diurnal bias. This correction methodology resulted in a significant

495 improvement in the GEMS SSA values within the expected error range. Thereby, it enhanced the overall accuracy of the SSA

496 retrieval. Variable importance analysis for the post-processing correction of the GEMS SSA was conducted (Figure S5). The

497 GEMS SSA was the most important variable in the correction process. The GEMS AOD also emerged as a highly influential

498 variable in the RF models for GEMS SSA post-process correction. Also, aerosol types appeared to have relatively lower

499 significance within the RF models for SSA correction.

501 5.3 Aerosol layer height

502 From November 1, 2021 to October 31, 2022, the GEMS and CALIOP data were co-located for comparison. In this section,

503 the level-2 aerosol extinction coefficients at 532 nm are used to calculate the CALIOP ALH. This is shown in Equation 2.

504 GEMS ALH pixels within a 0.05° radius surrounding each CALIOP pixel were averaged and compared with the CALIOP

505 ALHs within a time window of 1 h from the GEMS observation time. The validation was conducted when the GEMS AOD

506 values were larger than 0.2. This was because the error in ALH retrieval increased when the presence of aerosols in the

507 atmosphere was insufficient. Figure 11a shows a histogram of the differences between the GEMS and CALIOP ALH. The total

508 co-located number of data is 77,318, and the mean difference is -0.225 km. The median of differences is -0.167 km. This

509 indicates that the histogram distribution of the differences follows a Gaussian distribution although it is skewed marginally in

510 a positive direction. Figure 11b shows a comparison between the GEMS and CALIOP ALH. These were distributed

511 predominantly at altitudes less than 2 km. The percentage of data falling within the expected error of ±1 km was 55.3%, and

512 the percentage falling within the expected error of ±1.5 km was 71.7%. The variability of the GEMS ALH was comparable to

513 that of the CALIOP ALH.

515 6 Summary and future work

516 In this study, we present the first atmospheric aerosol monitoring results from GEMS over Asia. Given that the GEMS

517 AERAOD algorithm was developed using OMI as input data before GEMS launch, modifications were made considering the

518 GEO observation characteristics during the IOT period. A new hourly surface reflectance database was created using the

519 minimum reflectance method with a fine spatial resolution that aligned with the GEMS pixel resolution. In addition, monthly

520 BAOD maps were incorporated to estimate the hourly GEMS surface reflectance. A new cloud removal techniques

521 significantly improved effectiveness of cloud detection and enhanced the quality of aerosol retrievals. To avoid discrepancies

522 between observed and simulated radiance that may arise due to the monochromatic assumption of LUT calculation, we applied

523 a spectral binning approach to LUT calculation. Finally, post-process correction methods based on machine learning were used

524 to remove the non-physical diurnal biases in AOD and SSA retrieval. This reduced the biases over time and provided more

525 reliable hourly GEMS aerosol products in near real-time.

526 The GEMS aerosol product was investigated for three specific events: dust events over Northeast Asia, biomass burning in

527 Southeast Asia, and the absorption of aerosols over India. These events highlight the capability of the GEMS to monitor and

528 provide insights into aerosol properties during various atmospheric events while also emphasizing the importance of post-

529 processing for data accuracy and agreement with ground measurements.

530 The GEMS aerosol products were validated against the AERONET and CALIOP data for the entire GEMS domain for one

531 year (from November 2021 to October 2022). The performance of the GEMS aerosol algorithm was validated to verify its

532 applicability for studying the distribution of AOPs across Asia. The validation results for each product are summarized below:

533 GEMS AOD shows a good correlation with the AERONET AOD (R = 0.792). However, it exhibits certain bias patterns.

534 Notably, an underestimation of AOD in high AERONET AOD and overestimation of AOD in low AERONET AOD occurred

535 owing to cloud contamination. Different aerosol types exhibited varying validation results: the HAF type with the highest R

536 and Q values; the dust type with underestimation in India but overestimation in Northeast Asia; and NA type with cloud

537 contamination issues, particularly for low AOD. This indicated the need for an improvement in the cloud masking process,

538 particularly over the ocean. Certain deviations beyond the error range of the GEMS AOD were observed in India and Beijing.

539 The underestimation of the high AOD values can be attributed to the aerosol model. Diurnal variation in retrieval performance

540 was evident with varying slopes and other comparison statistics throughout the day. As the testbed for the GEMS algorithm

541 was on the LEO platform, the time-dependent retrieval bias had not been observed previously. Therefore, we adopted a model-

542 enforced post-process correction and find that this enhances GEMS AOD performance, reducing overall biases. This corrected

543 data ensures reliability for various applications.

544 The GEMS SSA at 443 nm was validated against the AERONET SSA at 440 nm over the entire GEMS region. The GEMS

545 SSA's agreement with the AERONET data was evaluated within a reasonable error range of ±0.03 (±0.05). For GEMS AOD

546 exceeding 0.4, 42.76 (67.25)% of GEMS SSA is within ±0.03 (0.05) error. This increases to 56.61 (85.70)% for strong aerosol

547 signals (GEMS AOD above 1.0). However, the accuracy varies among the aerosol types. The HAF type has a higher variability

548 and lower accuracy. The dust type has a marginal positive bias, particularly when the AOD is high. Similar to AOD, post-

549 process correction for the GEMS SSA data yielded significant enhancements in statistical metrics.

550 The GEMS and CALIOP data were then compared. The GEMS ALH was compared with the CALIOP ALH when the GEMS

551 AOD exceeded 0.2. The results showed a mean difference of -0.225 km, with 55.29% of data being within ±1 km and 71.70%

552 being within ±1.5 km. The GEMS ALH exhibited variability similar to that of CALIOP ALH.

553 Several methods can be used to further improve the results of the GEMS aerosol algorithm. First, additional satellite data could

554 be integrated for cloud detection. Incorporating data from other satellite sensors with IR channels such as the AMI can provide

555 complementary information for cloud masking. Second, it is necessary to consider the AOPs used in the LUT to improve the

556 GEMS aerosol algorithm. It is particularly important to incorporate more ground-based observations in the UV region, such

557 as those from the Pandora Instrument and SKYNET. Collecting ground-based observations in the UV region and incorporating

558 these into LUT can enhance the performance of this algorithm. Finally, regional LUTs with data from diverse regions that

559 consider the variability in AOPs based on regional characteristics are crucial. Overall, the improvements to the GEMS aerosol

560 algorithm contribute to advancing our understanding of aerosol properties and their effects on the environment. Thereby, it

561 provides valuable information for diverse applications including air quality monitoring, air quality data assimilation, and health

562 impact assessments in Asia.

563

564 *Code availability.* The GEMS L2 AERAOD algorithm is not available publicly.

565

568

569 *Author Contribution.* YC, JK, SG, and MK designed the experiments. WL and DL provided support for the data collection.
570 SL, MK, HC, OT, and SP contributed to the algorithm development. YC wrote the manuscript with contributions from all the
571 co-authors. JK reviewed and edited the manuscript. JK provided support and supervision. All the authors analyzed the
572 measurement data and prepared the manuscript.

573

576

583

586

587

References

588 References

589 Ahn, C., Torres, O., and Jethva, H.: Assessment of OMI near-UV aerosol optical depth over land, J. Geophys. Res. Atmos.,
590 119, 2457–2473, https://doi.org/10.1002/2013jd020188, 2014.

591 Ceamanos, X., Six, B., Moparthy, S., Carrer, D., Georgeot, A., Gasteiger, J., Riedi, J., Attié, J.-L., Lyapustin, A., and Katsev,
592 I.: Instantaneous aerosol and surface retrieval using satellites in geostationary orbit (iAERUS-GEO) – estimation of 15 min
593 aerosol optical depth from MSG/SEVIRI and evaluation with reference data, Atmos. Meas. Tech., 16, 2575–2599,
594 https://doi.org/10.5194/amt-16-2575-2023, 2023.

595 Choi, M., Kim, J., Lee, J., Kim, M., Park, Y.-J., Holben, B., Eck, T. F., Li, Z., and Song, C. H.: GOCI Yonsei aerosol retrieval
596 version 2 products: an improved algorithm and error analysis with uncertainty estimation from 5-year validation over East
597 Asia, Atmos. Meas. Tech., 11, 385–408, https://doi.org/10.5194/amt-11-385-2018, 2018.

598 Curier, R. L., Veefkind, J. P., Braak, R., Veihelmann, B., Torres, O., and de Leeuw, G.: Retrieval of aerosol optical properties
599 from OMI radiances using a multiwavelength algorithm: Application to western Europe. J. Geophys. Res. Atmos., 113(D17),
600 2008.

601 Dobber, M., Kleipool, Q., Dirksen, R., Levelt, P., Jaross, G., Taylor, S., Kelly, T., Flynn, L., Leppelmeier, G., and Rozemeijer,
602 N.: Validation of Ozone Monitoring Instrument level 1b data products, J. Geophys. Res., 113,
603 https://doi.org/10.1029/2007jd008665, 2008.

604 Dubovik, O. and King, M. D.: A flexible inversion algorithm for retrieval of aerosol optical properties from Sun and sky
605 radiance measurements, J. Geophys. Res., 105, 20673–20696, https://doi.org/10.1029/2000JD900282, 2000.

606 Giles, D. M., Sinyuk, A., Sorokin, M. G., Schafer, J. S., Smirnov, A., Slutsker, I., Eck, T. F., Holben, B. N., Lewis, J. R.,
607 Campbell, J. R., Welton, E. J., Korkin, S. V., and Lyapustin, A. I.: Advancements in the Aerosol Robotic Network (AERONET)
608 Version 3 database – automated near-real-time quality control algorithm with improved cloud screening for Sun photometer
609 aerosol optical depth (AOD) measurements, Atmos. Meas. Tech., 12, 169–209, https://doi.org/10.5194/amt-12-169-2019, 2019.

610 Go, S., Kim, J., Mok, J., Irie, H., Yoon, J., Torres, O., Krotkov, N. A., Labow, G., Kim, M., Koo, J.-H., Choi, M., and Lim, H.:
611 Ground-based retrievals of aerosol column absorption in the UV spectral region and their implications for GEMS
612 measurements, Remote Sens. Environ., 245, https://doi.org/10.1016/j.rse.2020.111759, 2020.

613 Go, S., Kim, J., Park, S. S., Kim, M., Lim, H., Kim, J.-Y., Lee, D.-W., and Im, J.: Synergistic Use of Hyperspectral UV-Visible
614 OMI and Broadband Meteorological Imager MODIS Data for a Merged Aerosol Product, Remote Sens., 12,
615 https://doi.org/10.3390/rs12233987, 2020.

616 Holben, B. N., Eck, T. F., Slutsker, I., Tanre, D., Buis, J. P., Setzer, A., Vermote, E., Reagan, J. A., Kaufman, Y., Nakajima, T.,
617 Lavenue, F., Jankowiak, I., and Smirnov, A.: AERONET – A federated instrument network and data archive for aerosol
618 characterization, Remote Sens. Environ., 66, 1–16, https://doi.org/10.1016/S0034-4257(98)00031-5, 1998.

619 Hsu, N. C., Lee, J., Sayer, A. M., Kim, W., Bettenhausen, C., and Tsay, S. C.: VIIRS Deep Blue Aerosol Products Over Land:
620 Extending the EOS Long-Term Aerosol Data Records, J. Geophys. Res. Atmos., 124, 4026–4053,
621 https://doi.org/10.1029/2018jd029688, 2019.

622 Hsu, N. C., Si-Chee, T., King, M. D., and Herman, J. R.: Aerosol properties over bright-reflecting source regions, IEEE Trans.
623 Geosci. Remote Sens., 42, 557–569, https://doi.org/10.1109/tgrs.2004.824067, 2004.

624 Hsu, N. C., Tsay, S. C., King, M. D., and Herman, J. R.: Deep Blue Retrievals of Asian Aerosol Properties During ACE-Asia,

Atmospheric
Measurement
Techniques
Discussions

Open Access

EGU

625   IEEE Trans. Geosci. Remote Sens., 44, 3180–3195, https://doi.org/10.1109/tgrs.2006.879540, 2006.

626   Jackson, J. M., Liu, H., Laszlo, I., Kondragunta, S., Remer, L. A., Huang, J., and Huang, H.-C.: Suomi-NPP VIIRS aerosol

627   algorithms and data products, J. Geophys. Res. Atmos., 118, 12,673–612,689, https://doi.org/10.1002/2013jd020449, 2013.

628   Jethva, H., Satheesh, S. K., and Srinivasan, J.: Assessment of second-generation MODIS aerosol retrieval (Collection 005) at

629   Kanpur, India, Geophys. Res. Lett., 34, https://doi.org/10.1029/2007gl029647, 2007.

630   Kalashnikova, O. V., Garay, M. J., Martonchik, J. V., and Diner, D. J.: MISR Dark Water aerosol retrievals: operational

631   algorithm sensitivity to particle non-sphericity, Atmos. Meas. Tech., 6, 2131–2154, https://doi.org/10.5194/amt-6-2131–2013,

632   2013.

633   Kang, M., Ahn, M.-H., Liu, X., Jeong, U., and Kim, J.: Spectral Calibration Algorithm for the Geostationary Environment

634   Monitoring Spectrometer (GEMS), Remote Sens., 12, https://doi.org/10.3390/rs12172846, 2020.

635   Kayetha, V., Torres, O., and Jethva, H.: Retrieval of UV–visible aerosol absorption using AERONET and OMI–MODIS

636   synergy: spatial and temporal variability across major aerosol environments, Atmos. Meas. Tech., 15, 845–877,

637   https://doi.org/10.5194/amt-15-845-2022, 2022.

638   Kim, J., Jeong, U., Ahn, M.-H., Kim, J. H., Park, R. J., Lee, H., Song, C. H., Choi, Y.-S., Lee, K.-H., Yoo, J.-M., Jeong, M.-J.,

639   Park, S. K., Lee, K.-M., Song, C.-K., Kim, S.-W., Kim, Y. J., Kim, S.-W., Kim, M., Go, S., Liu, X., Chance, K., Chan Miller,

640   C., Al-Saadi, J., Veihelmann, B., Bhartia, P. K., Torres, O., Abad, G. G., Haffner, D. P., Ko, D. H., Lee, S. H., Woo, J.-H.,

641   Chong, H., Park, S. S., Nicks, D., Choi, W. J., Moon, K.-J., Cho, A., Yoon, J., Kim, S.-k., Hong, H., Lee, K., Lee, H., Lee, S.,

642   Choi, M., Veefkind, P., Levelt, P. F., Edwards, D. P., Kang, M., Eo, M., Bak, J., Baek, K., Kwon, H.-A., Yang, J., Park, J., Han,

643   K. M., Kim, B.-R., Shin, H.-W., Choi, H., Lee, E., Chong, J., Cha, Y., Koo, J.-H., Irie, H., Hayashida, S., Kasai, Y., Kanaya,

644   Y., Liu, C., Lin, J., Crawford, J. H., Carmichael, G. R., Newchurch, M. J., Lefer, B. L., Herman, J. R., Swap, R. J., Lau, A. K.

645   H., Kurosu, T. P., Jaross, G., Ahlers, B., Dobber, M., McElroy, C. T., and Choi, Y.: New Era of Air Quality Monitoring from

646   Space: Geostationary Environment Monitoring Spectrometer (GEMS), Bull. Am. Meteorol. Soc., 101, E1–E22,

647   https://doi.org/10.1175/bams-d-18-0013.1, 2020.

648   Kim, M., Kim, J., Jeong, U., Kim, W., Hong, H., Holben, B., Eck, T. F., Lim, J. H., Song, C. K., Lee, S., and Chung, C. Y.:

649   Aerosol optical properties derived from the DRAGON-NE Asia campaign, and implications for a single-channel algorithm to

650   retrieve aerosol optical depth in spring from Meteorological Imager (MI) on-board the Communication, Ocean, and

651   Meteorological Satellite (COMS), Atmos. Chem. Phys., 16, 1789–1808, https://doi.org/10.5194/acp-16-1789-2016, 2016.

652   Kim, M., Kim, J., Torres, O., Ahn, C., Kim, W., Jeong, U., Go, S., Liu, X., Moon, K., and Kim, D.-R.: Optimal Estimation-

653   Based Algorithm to Retrieve Aerosol Optical Properties for GEMS Measurements over Asia, Remote Sens., 10,

654   https://doi.org/10.3390/rs10020162, 2018.

655   Kim, M., Kim, S. H., Kim, W. V., Lee, Y. G., Kim, J., and Kafatos, M. C.: Assessment of Aerosol optical depth under

656   background and polluted conditions using AERONET and VIIRS datasets, Atmos. Environ., 245,

657   https://doi.org/10.1016/j.atmosenv.2020.117994, 2021.

658   Kleipool, Q. L., Dobber, M. R., de Haan, J. F., and Levelt, P. F.: Earth surface reflectance climatology from 3 years of OMI

659   data, J. Geophys. Res., 113, https://doi.org/10.1029/2008jd010290, 2008.

660   Kondragunta, S., Laszlo, I., Zhang, H., Ciren, P., and Huff, A.: Air Quality Applications of ABI Aerosol Products from the

661   GOES-R Series, in: The GOES-R Series: A New Generation of Geostationary Environmental Satellites, Elsevier, Amsterdam,

662   the Netherlands, Oxford, UK, Cambridge MA, USA, 203–217, 2020.

Atmospheric
Measurement
Techniques
Discussions

663   Lee, S., Choi, M., Kim, J., Park, Y. J., Choi, J. K., Lim, H., Lee, J., Kim, M., and Cho, Y.: Retrieval of aerosol optical properties
664   from GOCI-II observations: Continuation of long-term geostationary aerosol monitoring over East Asia, Sci. Total Environ.,
665   903, 166504, https://doi.org/10.1016/j.scitotenv.2023.166504, 2023.

666   Lee, Y., Ahn, M.-H., Kang, M., and Eo, M.: Spectral replacement using machine learning methods for continuous mapping of
667   the Geostationary Environment Monitoring Spectrometer (GEMS), Atmos. Meas. Tech., 16, 153–168,
668   https://doi.org/10.5194/amt-16-153-2023, 2023.

669   Lennartson, E. M., Wang, J., Gu, J., Castro Garcia, L., Ge, C., Gao, M., Choi, M., Saide, P. E., Carmichael, G. R., Kim, J., and
670   Janz, S. J.: Diurnal variation of aerosol optical depth and PM2.5 in South Korea: a synthesis from AERONET, satellite (GOCI),
671   KORUS-AQ observation, and the WRF-Chem model, Atmos. Chem. Phys., 18, 15125–15144, https://doi.org/10.5194/acp-18-
672   15125-2018, 2018.

673   Levelt, P. F., van den Oord, G. H. J., Dobber, M. R., Malkki, A., Huib, V., Johan de, V., Stammes, P., Lundell, J. O. V., and
674   Saari, H.: The ozone monitoring instrument, IEEE Trans. Geosci. Remote Sens., 44, 1093–1101,
675   https://doi.org/10.1109/tgrs.2006.872333, 2006.

676   Levelt, P. F., Joiner, J., Tamminen, J., Veefkind, J. P., Bhartia, P. K., Stein Zweers, D. C., Duncan, B. N., Streets, D. G., Eskes,
677   H., van der A, R., McLinden, C., Fioletov, V., Carn, S., de Laat, J., DeLand, M., Marchenko, S., McPeters, R., Ziemke, J., Fu,
678   D., Liu, X., Pickering, K., Apituley, A., González Abad, G., Arola, A., Boersma, F., Chan Miller, C., Chance, K., de Graaf, M.,
679   Hakkarainen, J., Hassinen, S., Ialongo, I., Kleipool, Q., Krotkov, N., Li, C., Lamsal, L., Newman, P., Nowlan, C., Suleiman,
680   R., Tilstra, L. G., Torres, O., Wang, H., and Wargan, K.: The Ozone Monitoring Instrument: overview of 14 years in space,
681   Atmos. Chem. Phys., 18, 5699–5745, https://doi.org/10.5194/acp-18-5699-2018, 2018.

682   Levy, R. C., Mattoo, S., Munchak, L. A., Remer, L. A., Sayer, A. M., Patadia, F., and Hsu, N. C.: The Collection 6 MODIS
683   aerosol products over land and ocean, Atmos. Meas. Tech., 6, 2989–3034, https://doi.org/10.5194/amt-6-2989-2013, 2013.

684   Lipponen, A., Kolehmainen, V., Kolmonen, P., Kukkurainen, A., Mielonen, T., Sabater, N., Sogacheva, L., Virtanen, T. H., and
685   Arola, A.: Model-enforced post-process correction of satellite aerosol retrievals, Atmos. Meas. Tech., 14, 2981–2992,
686   https://doi.org/10.5194/amt-14-2981-2021, 2021.

687   Lipponen, A., Reinvall, J., Väisänen, A., Taskinen, H., Lähivaara, T., Sogacheva, L., Kolmonen, P., Lehtinen, K., Arola, A.,
688   and Kolehmainen, V.: Deep-learning-based post-process correction of the aerosol parameters in the high-resolution Sentinel-
689   3 Level-2 Synergy product, Atmos. Meas. Tech., 15, 895–914, https://doi.org/10.5194/amt-15-895-2022, 2022.

690   Lyapustin, A., Wang, Y., Go, S., Choi, M., Korkin, S., Huang, D., Knyazikhin, Y., Blank, K., and Marshak, A.: Atmospheric
691   Correction of DSCOVR EPIC: Version 2 MAIAC Algorithm, Front. Remote Sens., 2,
692   https://doi.org/10.3389/frsen.2021.748362, 2021.

693   Lyapustin, A., Wang, Y., Korkin, S., and Huang, D.: MODIS Collection 6 MAIAC algorithm, Atmos. Meas. Tech., 11, 5741–
694   5765, https://doi.org/10.5194/amt-11-5741-2018, 2018.

695   Nanda, S., de Graaf, M., Veefkind, J. P., Sneep, M., ter Linden, M., Sun, J., and Levelt, P. F.: A first comparison of TROPOMI
696   aerosol layer height (ALH) to CALIOP data, Atmos. Meas. Tech., 13, 3043–3059, https://doi.org/10.5194/amt-13-3043-2020,
697   2020.

698   Park, S. S., Kim, J., Cho, Y., Lee, H., Park, J., Lee, D.-W., Lee, W.-J., and Kim, D.-R.: Retrieval Algorithm for Aerosol Effective
699   Height from the Geostationary Environment Monitoring Spectrometer (GEMS), Atmos. Meas. Tech. Discuss., https://doi.org/
700   10.5194/amt-223-136.

701 Powell, K. A., Hu, Y., Omar, A., Vaughan, M. A., Winker, D. M., Liu, Z., Hunt, W. H., and Young, S. A.: Overview of the

702 CALIPSO Mission and CALIOP Data Processing Algorithms, J. Atmos. Ocean. Tech., 26, 2310–2323,

703 https://doi.org/10.1175/2009jtecha1281.1, 2009.

704 Ram, K., Sarin, M.M., Sudheer, A.K., and Rengarajan, R.: Carbonaceous and Secondary Inorganic Aerosols during Wintertime

705 Fog and Haze over Urban Sites in the Indo-Gangetic Plain, Aerosol Air Qual. Res., 41, 359–370,

706 https://doi.org/10.4209/aaqr.2011.07.0105, 2012.

707 Sayer, A. M., Hsu, N. C., Lee, J., Carletta, N., Chen, S. H., and Smirnov, A.: Evaluation of NASA Deep Blue/SOAR aerosol

708 retrieval algorithms applied to AVHRR measurements, J. Geophys. Res. Atmos., 122, 9945–9967,

709 https://doi.org/10.1002/2017JD026934, 2017.

710 Singh, G. K., Choudhary, V., Rajeev, P., Paul, D., and Gupta, T.: Understanding the origin of carbonaceous aerosols during

711 periods of extensive biomass burning in northern India. Environ. Pollut., 270, 116082,

712 https://doi.org/10.1016/j.envpol.2020.116082, 2021.

713 Sinyuk, A., Holben, B. N., Eck, T. F., Giles, D. M., Slutsker, I., Korkin, S., Schafer, J. S., Smirnov, A., Sorokin, M., and

714 Lyapustin, A.: The AERONET Version 3 aerosol retrieval algorithm, associated uncertainties and comparisons to Version 2,

715 Atmos. Meas. Tech., 13, 3375–3411, https://doi.org/10.5194/amt-13-3375-2020, 2020.

716 Spurr, R. J. D.: VLIDORT: A linearized pseudo-spherical vector discrete ordinate radiative transfer code for forward model

717 and retrieval studies in multilayer multiple scattering media, J. Quant. Spectrosc. Radiat. Transf., 102, 316–342,

718 https://doi.org/10.1016/j.jqsrt.2006.05.005, 2006.

719 Taskinen, H., Väisänen, A., Hatakka, L., Virtanen, T. H., Lähivaara, T., Arola, A., Kolehmainen, V., and Lipponen, A.: High-

720 Resolution Post-Process Corrected Satellite AOD, Geophys. Res. Lett., 49, https://doi.org/10.1029/2022gl099733, 2022.

721 Torres, O., Bhartia, P. K., Herman, J. R., Syniuk, A., Ginoux, P., and Holben, B.: A long term record of aerosol optical depth

722 from TOMS observations D and comparison to AERONET measurements, J. Atm. Sci., 59, 398–413, 2002.

723 Torres, O., Ahn, C., and Chen, Z.: Improvements to the OMI near-UV aerosol algorithm using A-train CALIOP and AIRS

724 observations, Atmos. Meas. Tech., 6, 3257–3270, https://doi.org/10.5194/amt-6-3257-2013, 2013.

725 Torres, O., Bhartia, P. K., Sinyuk, A., Welton, E. J., and Holben, B.: Total Ozone Mapping Spectrometer measurements of

726 aerosol absorption from space: Comparison to SAFARI 2000 ground-based observations, J. Geophys. Res., 110, D10S18,

727 https://doi.org/10.1029/2004JD004611, 2005.

728 Torres, O., Tanskanen, A., Veihelmann, B., Ahn, C., Braak, R., Bhartia, P. K., Veefkind, P., and Levelt, P.: Aerosols and surface

729 UV products from Ozone Monitoring Instrument observations: An overview, J. Geophys. Res., 112,

730 https://doi.org/10.1029/2007jd008809, 2007.

731 Torres, O., Jethva, H., Ahn, C., Jaross, G., and Loyola, D. G.: TROPOMI aerosol products: evaluation and observations of

732 synoptic-scale carbonaceous aerosol plumes during 2018–2020, Atmos. Meas. Tech., 13, 6789–6806,

733 https://doi.org/10.5194/amt-13-6789–2020, 2020.

734 Wei, J., Li, Z., Sun, L., Peng, Y., Zhang, Z., Li, Z., Su, T., Feng, L., Cai, Z., and Wu, H.: Evaluation and uncertainty estimate

735 of next-generation geostationary meteorological Himawari-8/AHI aerosol products, Sci. Total Environ., 692, 879–891,

736 https://doi.org/10.1016/j.scitotenv.2019.07.326, 2019.

737 Xu, X., Wang, J., Wang, Y., Zeng, J., Torres, O., Reid, J. S., Miller, S. D., Martins, J. V., and Remer, L. A.: Detecting layer

738   height of smoke aerosols over vegetated land and water surfaces via oxygen absorption bands: hourly results from

739   EPIC/DSCOVR in deep space, Atmos. Meas. Tech., 12, 3269–3288, https://doi.org/10.5194/amt-12-3269-2019, 2019.

740   Xu, X., Wang, J., Wang, Y., Zeng, J., Torres, O., Yang, Y., Marshak, A., Reid, J., and Miller, S.: Passive remote sensing of

741   altitude and optical depth of dust plumes using the oxygen A and B bands: first results from EPIC/DSCOVR at Lagrange-1

742   point, Geophys. Res. Lett., 44, 7544–7554, https://doi.org/10.1002/2017gl073939, 2017.

743   Yin, S., Wang, X., Zhang, X., Guo, M., Miura, M., and Xiao, Y.: Influence of biomass burning on local air pollution in mainland

744   Southeast Asia from 2001 to 2016, Environ. Pollut., 254, 112949, https://doi.org/10.1016/j.envpol.2019.07.117, 2019.

745   Yoshida, M., Kikuchi, M., Nagao, T. M., Murakami, H., Nomaki, T., and Higurashi, A.: Common Retrieval of Aerosol

746   Properties for Imaging Satellite Sensors, J. Meteorol. Soc. Jpn. Ser. II, 96B, 193–209, https://doi.org/10.2151/jmsj.2018-039,

747   2018.

748   Zhang, H., Kondragunta, S., Laszlo, I., and Zhou, M.: Improving GOES Advanced Baseline Imager (ABI) aerosol optical

749   depth (AOD) retrievals using an empirical bias correction algorithm, Atmos. Meas. Tech., 13, 5955–5975,

750   https://doi.org/10.5194/amt-13-5955–2020, 2020.

751   Zhang, H., Kondragunta, S., Laszlo, I., Liu, H., Remer, L. A., Huang, J., Superczynski, S., and Ciren, P.: An enhanced VIIRS

752   aerosol optical thickness (AOT) retrieval algorithm over land using a global surface reflectance ratio database, J. Geophys.

753   Res. Atmos., 121, https://doi.org/10.1002/2016jd024859, 2016.

754   Zhang, W., Gu, X., Xu, H., Yu, T., and Zheng, F.: Assessment of OMI near-UV aerosol optical depth over Central and East

755   Asia, J. Geophys. Res. Atmos., 121, 382–398, https://doi.org/10.1002/2015jd024103, 2016.

756   Zhang, Z., Wu, W., Fan, M., Tao, M., Wei, J., Jin J., Tan, Y. and Wang, Q.: Validation of Himawari-8 aerosol optical depth

757   retrievals over China, Atmos. Environ., 199, https://doi.org/10.1016/j.atmosenv.2018.11.024, 2019.

758

759
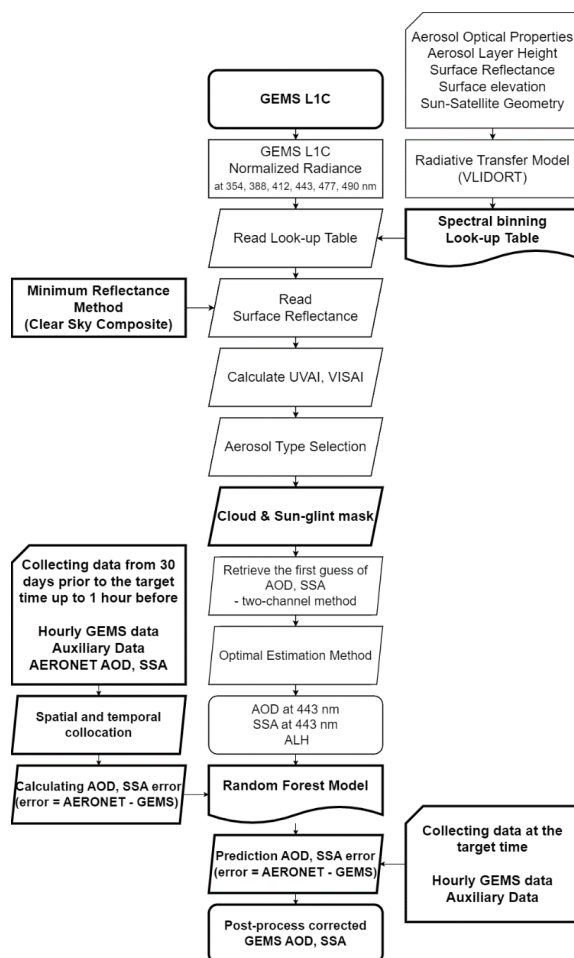
Figure 1: The flowchart of the GEMS AERAOD retrieval algorithm and the modifications in the study (in bold boxes)
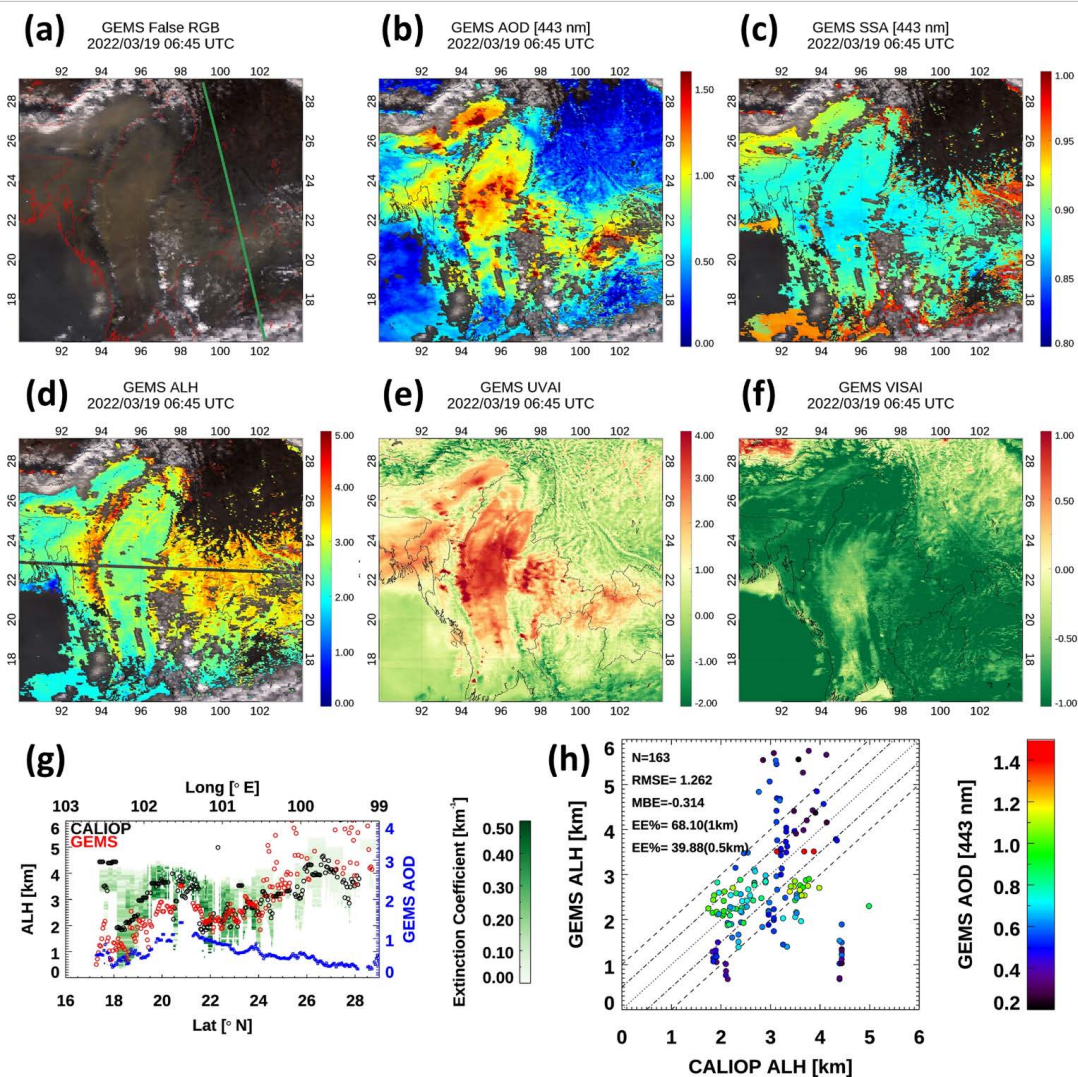
761
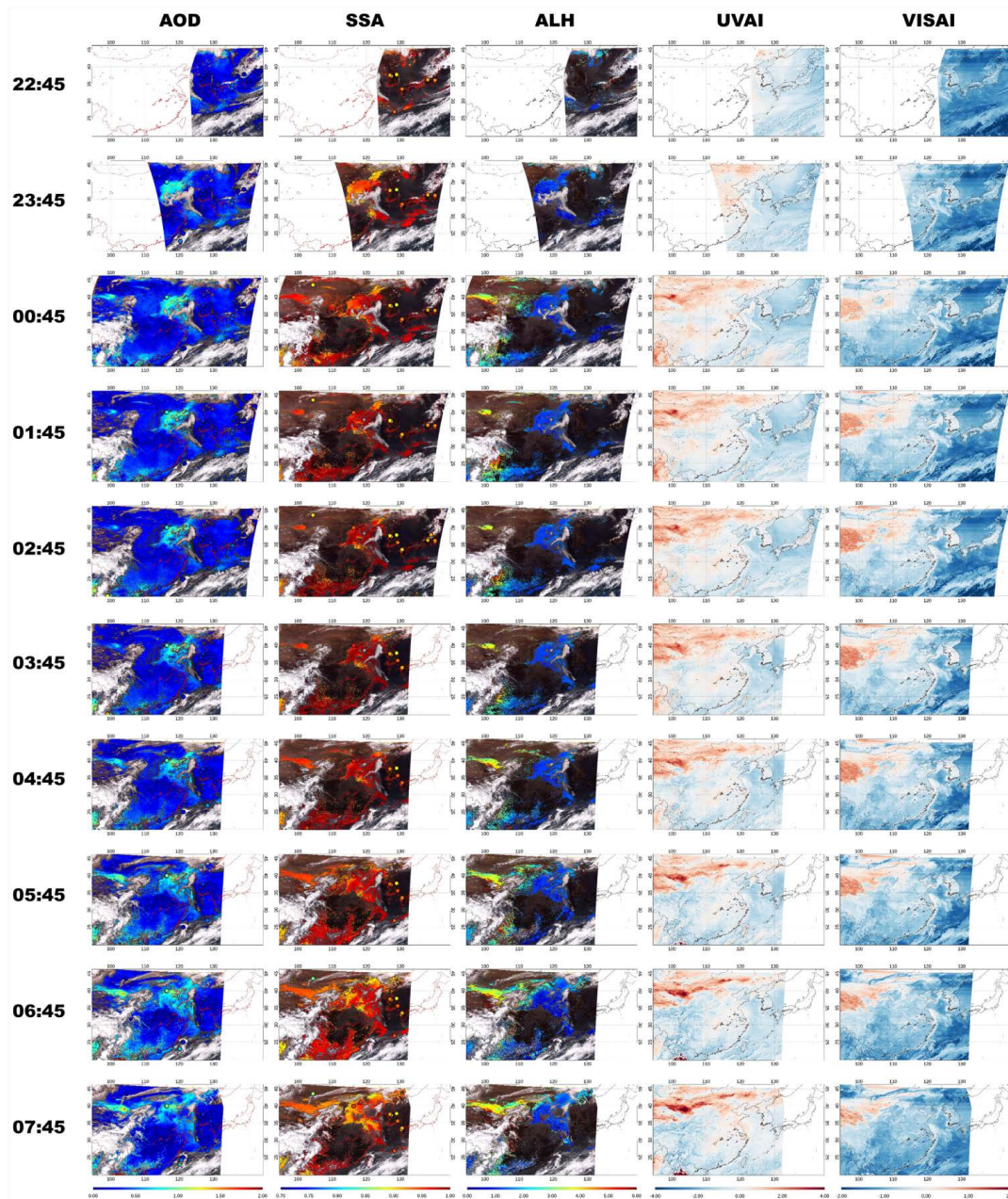
Figure 2: Hourly GEMS aerosol products for the dust case on April 8, 2022 over northwestern China. Time-series maps of AOD, SSA, ALH, UVAI, and VISAI from 22:45 to 07:45. The circle denotes an AERONET station, and the filled color indicates the AERONET AOD and SSA at 443 nm in the AOD and SSA columns. GEMS SSA, and ALH are displayed only when GEMS AOD > 0.2.

768

Figure 3: The example of GEMS aerosol products for biomass burning over mainland Southeast Asia. The maps of (a) GEMS False RGB, (b) AOD, (c) SSA, (d) ALH, (e) UVAI, and (f) VisAI. The green line in GEMS False RGB indicates the overpass path of CALIOP. The GEMS SSA and ALH are displayed only when the GEMS AOD is over 0.2. (g) GEMS ALH compared with CALIOP extinction coefficient in the domain. The background color represents the CALIOP extinction coefficient. The black open circles denote the CALIOP ALH, whereas the red open circles represent the GEMS ALH. The blue squares represent the GEMS AOD. (h) Comparison of GEMS and CALIOP ALH when GEMS AOD > 0.2. The dashed and dash-dotted lines indicate an uncertainty envelope of ±1 km and ±0.5 km in ALH, respectively. The dotted lines represent the 1:1 line. The color in the circles represents the GEMS AOD.

777

778

779
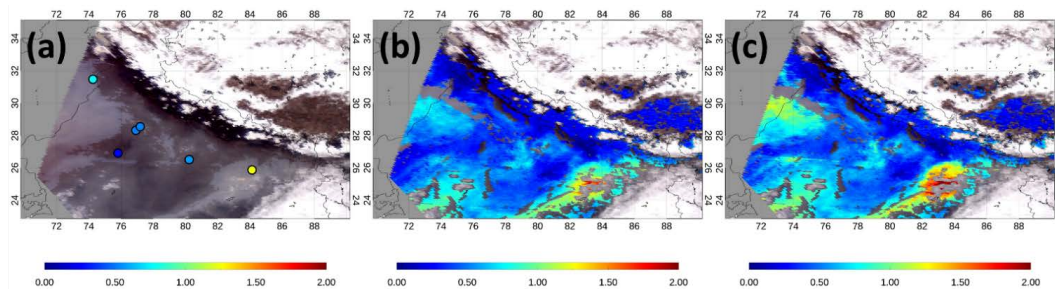
Figure 4: The example of the GEMS AOD before and after post-processing for an absorbing aerosol case over Indo-Gangatic Plane at 04:45 UTC on December 4, 2021. (a) GEMS false RGB. The circle denotes an AERONET station, and the filled color indicates the AERONET AOD at 443 nm, (b) GEMS AOD and (c) GEMS AOD after post-process correction.

783

784
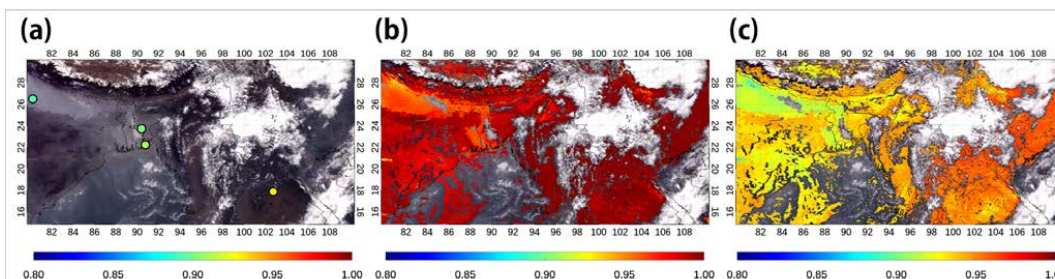
Figure 5: The example of GEMS SSA and the GEMS SSA after post-processing for an absorbing aerosol case over India, Bangladesh, and mainland Southeast Asia at 03:45 UTC on December 23, 2021. (a) GEMS false RGB. The circle denotes an AERONET station, and the filled color indicates the AERONET SSA at 440 nm, (b) GEMS SSA, and (c) GEMS SSA after post-process correction.

789

Atmospheric
Measurement
Techniques

Open Access

Discussions

EGU

AERONET sites used for the GEMS AOD and SSA validation
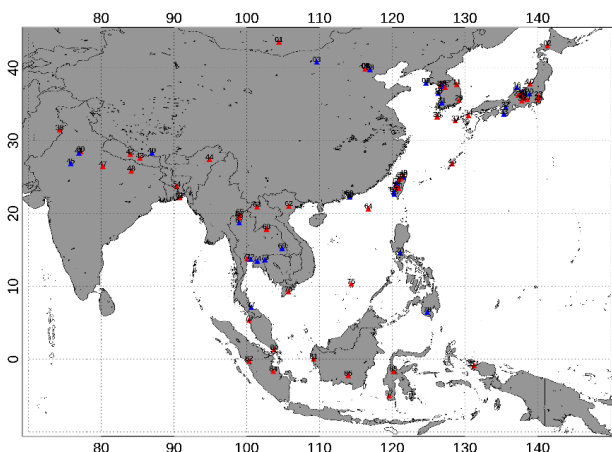
01:Dalanzadgad(915, 686)
02:Hokkaido_University(345, 188)
03:AOE_Baotou(828, 0)
04:Beijing_RADI(1229, 0)
05:Beijing_PKU(464, 222)
06:Beijing(1099, 0)
07:Beijing-CAMS(1469,1154)
08:XiangHe(719, 0)
09:Baengnyeong(427, 0)
10:Niigata(342, 197)
11:Gangneung_WNU(1260, 759)
12:Incheon(422, 303)
13:Yonsei_University(1053, 781)
14:Seoul_SNU(1046, 0)
15:Hankuk_UFS(997, 501)
16:Noto(299, 0)
17:DRAGON_Hakuba(5, 0)
18:Anmyon(958, 0)
19:DRAGON_Omachi(7, 2)
20:DRAGON_Mt_Haruna(2, 0)
21:DRAGON_Takayama(31, 12)
22:DRAGON_Matsumoto(377, 301)
23:TGF_Tsukuba(215, 174)
24:DRAGON_Suwa(10, 6)
25:DRAGON_Minowa(74, 49)
26:DRAGON_Ina(71, 51)
27:DRAGON_Kofu(301, 223)
28:Chiba_University(471, 336)
29:KORUS_UNIST_Ulsan(1245, 861)
30:DRAGON_Iida(72, 35)
31:Gwangju_GIST(603, 0)
32:Osaka(383, 0)
33:Shirahama(574, 0)
34:Fukuoka(1002, 515)
35:Gosan_NIMS_SNU(148, 94)
36:Gosan_SNU(293, 101)
37:Fukue(241, 129)
38:Lahore(842, 629)
39:IIT_Delhi(579, 456)
40:QOMS_CAS(326, 0)
41:Amity_Univ_Gurgaon(586, 0)
42:Pokhara(399, 249)
43:ICIMOD(107, 77)
44:Dibrugarh_Univ(473, 301)

45:Jaipur(54, 0)
46:Okinawa_Hedo(802, 285)
47:Kanpur(610, 447)
48:Gandhi_College(411, 275)
49:Cape_Fuguei_Station(208, 87)
50:Taipei_CWB(433, 0)
51:EPA-NCU(757, 296)
52:TASA_Taiwan(771, 325)
53:Xitun(563, 0)
54:Dhaka_University(636, 370)
55:Doulu(1033, 403)
56:Lulin(576, 159)
57:Chen-Kung_Univ(807, 0)
58:Kaohsiung(818, 0)
59:Hong_Kong_Sheung(30, 0)
60:Hong_Kong_PolyU(597, 0)
61:Bhola(488, 304)
62:NGHIA_DO(182, 66)
63:Luang_Namtha(282, 60)
64:Dongsha_Island(219, 85)
65:Doi_Ang_Khang(436, 210)
66:Chiang_Dao(576, 145)
67:Chiang_Mai_Met_Sta(806, 0)
68:Nong_Khai(604, 256)
69:Ubon_Ratchathani(1, 0)
70:Manila_Observatory(28, 0)
71:Silpakorn_Univ(530, 180)
72:Bangkok(256, 0)
73:Sra_Kaeo(397, 0)
74:Chachoengsao(321, 0)
75:Tai_Ping(50, 9)
76:Bac_Lieu(236, 24)
77:Songkhla_Met_Sta(110, 0)
78:ND_Marbel_Univ(281, 0)
79:USM_Penang(350, 88)
80:Singapore(413, 64)
81:Pontianak(780, 133)
82:Bukit_Kototabang(283, 59)
83:Sorong(166, 20)
84:Jambi(222, 3)
85:BMKG_GAW_PALU(130, 10)
86:Palangkaraya(400, 33)
87:Makassar(130, 8)

Figure 6: AERONET sites used for the GEMS AOD and SSA validation. The red color indicates the site where validation points exist for both AOD and SSA. The blue color indicates the site where validation points exist only for AOD. The list of station names in conjunction with the number of AERONET AOD and SSA data points for validation at each station.
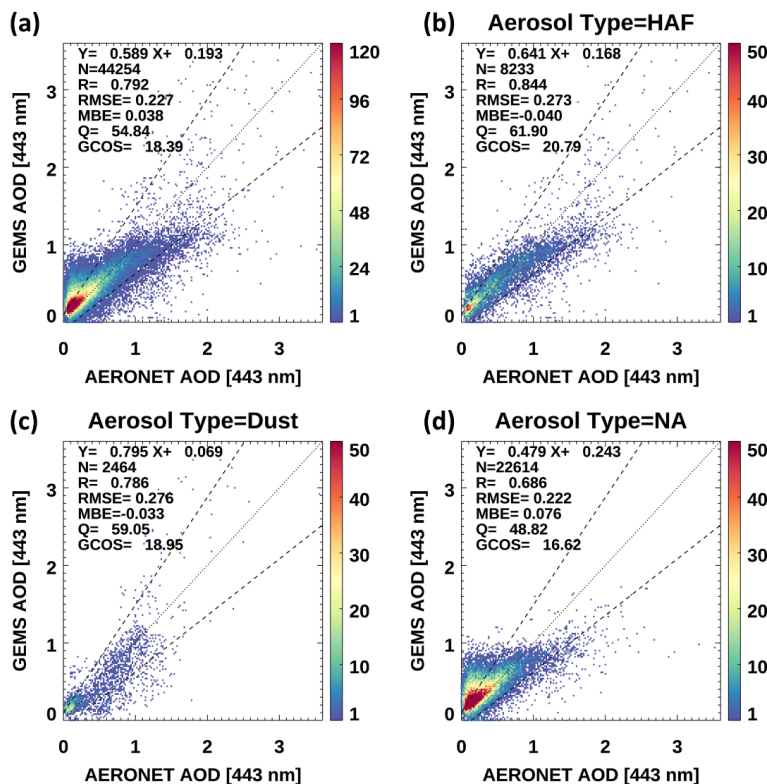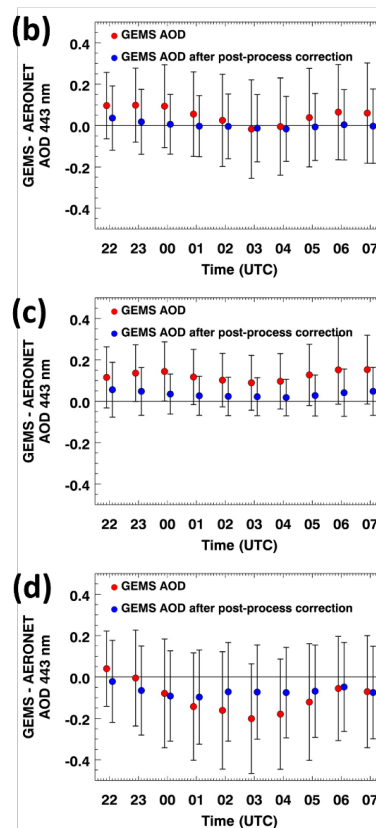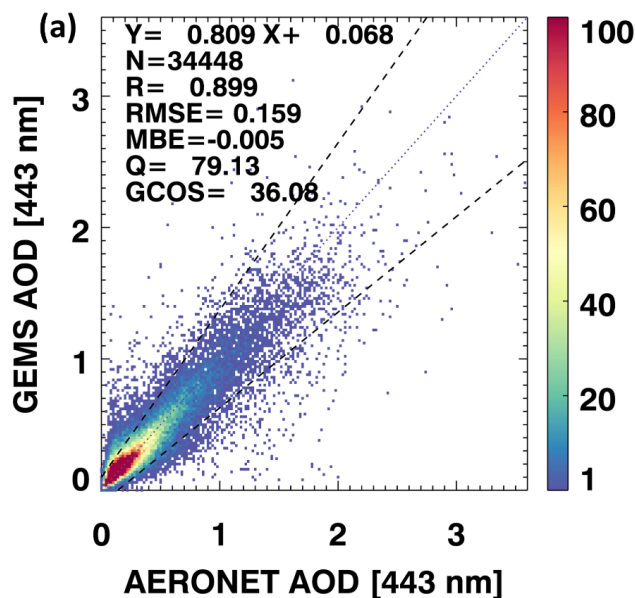

Figure 7: Comparison of GEMS and AERONET AOD for (a) total and individual aerosol types: (b) HAF, (c) dust, and (d) NA. The dashed lines indicate an uncertainty envelope of maximum (0.1 or 30%) in AOD. The dotted lines represent the 1:1 line. Data from November 1, 2021 to October 31, 2022 are used for comparison.

Atmospheric
Measurement
Techniques
Discussions

Open Access

EGU

799

Figure 8: (a) Comparison of GEMS AOD after post-process correction by machine learning and AERONET AOD. The dashed lines indicate an uncertainty envelope of a larger 0.1 or ±30% in AOD. The dotted lines represent the 1:1 line. The difference between GEMS AOD and AERONET AOD in terms of time. (b) All pixels, (c) pixels when AERONET AOD < 0.4, and (d) pixels when AERONET AOD > 0.4. The red circles represent the GEMS AOD, and the blue circles represent the GEMS AOD after post-process correction. The error bars correspond to the standard deviation. Data from December 1, 2021 to October 31, 2022 are used for comparison.

807
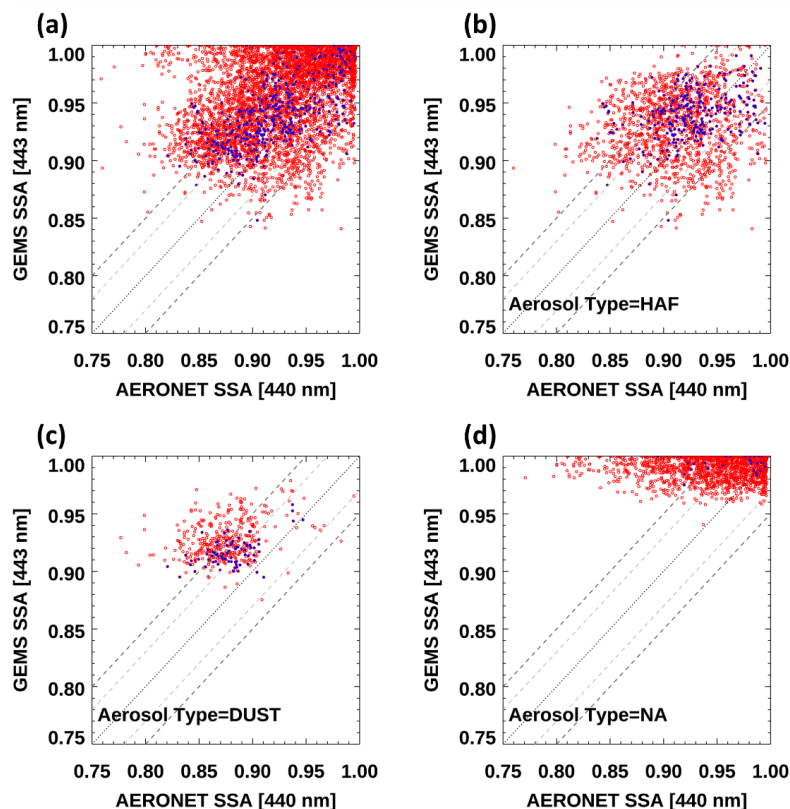
Figure 9: Comparison of GEMS and AERONET SSA for (a) total and individual aerosol types: (b) HAF, (c) dust, and (d) NA. The red circles represent the pixels when AOD > 0.4, and the blue circles represent the pixels when AOD > 1.0. The gray dashed lines indicate an uncertainty envelope of ±0.03 in SSA, the black dashed lines indicate an uncertainty envelope of ±0.05 in SSA, and the dotted lines represent the 1:1 line. Data from November 1, 2021 to October 31, 2022 are used for comparison.
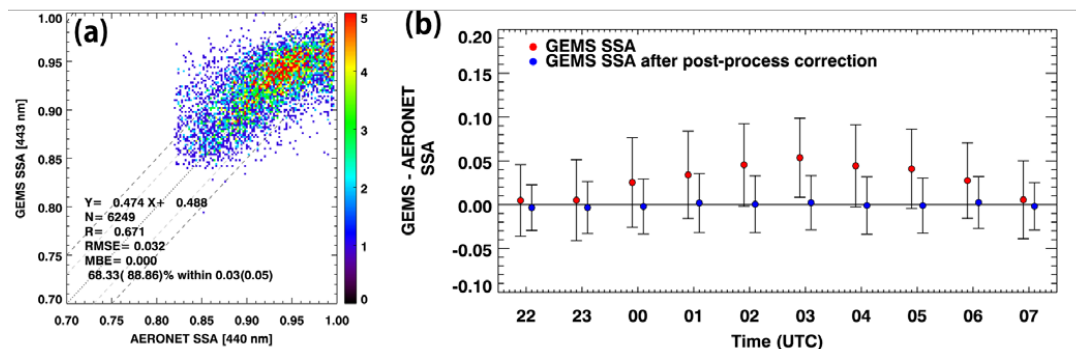
Figure 10: (a) Comparison of GEMS SSA after post-process correction and AERONET SSA. The gray dashed lines indicate an uncertainty envelope of ±0.03 in SSA, the black dashed lines indicate an uncertainty envelope of ±0.05 in SSA, and the dotted lines represent the 1:1 line. (b) The difference between GEMS and AERONET SSA in terms of time. Data from December 1, 2021 to October 31, 2022 are used for comparison.

Atmospheric
Measurement
Techniques
Discussions

820

Figure 11: (a) Histogram of difference between GEMS and CALIOP ALH and (b) comparison of GEMS and CALIOP ALH. The dashed lines indicate an uncertainty envelope of ±1 km in ALH. The dash-dotted lines indicate an uncertainty envelope of ±1.5 km in ALH. The dotted lines represent the 1:1 line. Data from November 1, 2021 to October 31, 2022 are used for comparison.
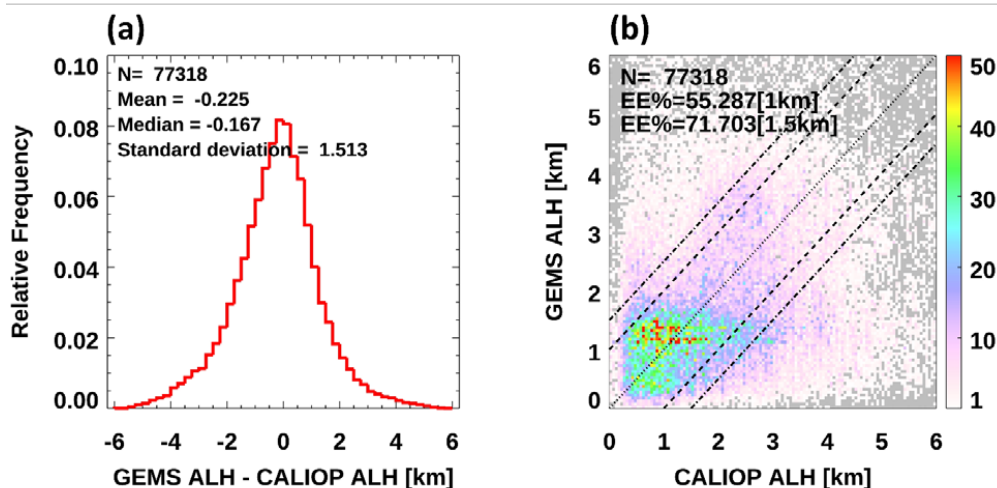
824

825 **Table 1: Dimension of LUT in GEMS Aerosol algorithm.**

Variable Name [Unit]	Number of Entries	Entries
Wavelength [nm]	6	354, 388, 412, 443, 477, 490
SZA [°]	12	0.01, 5, 10, 15, 20, 27, 34, 41, 48, 55, 62, 69
VZA [°]	12	0.01, 5, 10, 15, 20, 27, 34, 41, 48, 55, 62, 69
RAA [°]	11	0.01, 15, 30, 45, 60, 80, 100, 120, 140, 160, 180
Surface reflectance [-]	4	0.0, 0.05, 0.1, 0.2
AOD at 443 nm [-]	8	0.0, 0.1, 0.4, 0.8, 1.5, 2.0, 2.8, 3.6, 5.0, 10.0
SSA at 443 nm [-]	8	1.0, 0.98, 0.96, 0.94, 0.91, 0.88, 0.85, 0.82 for HAF and Dust 1.0, 0.99, 0.98, 0.97, 0.96, 0.94, 0.92, 0.90 for NA
ALH above the surface [km]	5	0.5, 1.5, 3.0, 4.5, 6.0
Elevation [km]	3	0, 3, 6

826

827 **Table 2: Statistic of hourly comparison of GEMS and AERONET AOD in Figure S2.**

Time	N	Slope	y-intercept	R	RMSE	MBE	Q (%)	GCOS (%)
22:45	925	0.730	0.180	0.715	0.188	0.100	58.38	23.24
23:45	1964	0.684	0.190	0.830	0.212	0.076	59.32	20.93
00:45	4593	0.584	0.217	0.767	0.224	0.088	51.32	16.74
01:45	5632	0.534	0.200	0.774	0.211	0.054	54.83	17.47
02:45	6400	0.555	0.183	0.795	0.221	0.029	54.53	18.55
03:45	6139	0.569	0.165	0.824	0.233	-0.013	56.54	17.04
04:45	6157	0.593	0.169	0.822	0.230	0.000	55.19	18.16
05:45	5642	0.586	0.204	0.773	0.235	0.041	52.87	19.25
06:45	4261	0.647	0.218	0.794	0.233	0.065	54.89	19.46
07:45	2541	0.617	0.224	0.771	0.247	0.054	56.55	19.48

828

829

830

831 **Table 3: Comparison of GEMS and AERONET SSA for different aerosol types in Figure 9. N represents the number of data, and**
832 **EE% denotes the percentage within the expected error range of ±0.03 (±0.05).**

	GEMS AOD > 0.4		GEMS AOD > 1.0	
Aerosol Type	N	EE% ±0.03 (±0.05)	N	EE% ±0.03 (±0.05)
All	5227	42.76(67.25)	454	56.61(83.70)
HAF	1559	41.95(70.24)	277	61.01(87.73)
Dust	437	20.37(50.57)	82	39.02(73.17)
NA	1850	45.14(65.62)	31	51.61(70.97)

833

834 **Table 4: Statistic of comparison of GEMS and AERONET SSA in Figure S4.**

	GEMS AOD > 0.4		GEMS AOD > 1.0	
Time	N	EE% ±0.03 (±0.05)	N	EE% ±0.03 (±0.05)
22:45	137	64.96 (86.13)	23	52.17 (86.96)
23:45	288	60.76 (83.68)	67	74.63 (92.54)
00:45	420	57.62 (82.38)	93	73.12 (88.17)
01:45	454	56.61 (79.07)	113	63.72 (88.50)
02:45	655	39.69 (62.90)	237	45.99 (73.00)
03:45	859	27.82 (53.20)	339	25.07 (57.23)
04:45	822	28.22 (55.60)	335	27.76 (62.39)
05:45	621	36.88 (63.12)	222	38.29 (67.57)
06:45	620	48.23 (73.23)	255	51.37 (77.65)
07:45	351	60.68 (79.49)	160	63.12 (84.38)

835